Development of a REgion-Specific Ecosystem Feedback Fire (RESFire) Model in the Community Earth System Model

Yufei Zou[1,2] (iD), Yuhang Wang[1] (iD), Ziming Ke[1], Hanqin Tian[3] (iD), Jia Yang[3] (iD), and Yongqiang Liu[4] (iD)

[1]School of Earth and Atmospheric Sciences, Georgia Institute of Technology, Atlanta, GA, USA, [2]Now at School of Environmental and Forest Sciences, University of Washington, Seattle, WA, USA, [3]International Center for Climate and Global Change Research, School of Forestry and Wildlife Sciences, Auburn University, Auburn, AL, USA, [4]Center for Forest Disturbance Science, USDA-Forest Service, Forestry Sciences Laboratory, Athens, GA, USA

Abstract Fires play a critical role in modulating regional and global climate through disturbances on meteorological, biogeochemical, and hydrological processes, while fires are strongly affected by climate, terrestrial ecosystems, and human activities. The complex climate-fire-ecosystem interactions with anthropogenic disturbance are not well understood. We developed a REgion-Specific ecosystem feedback Fire (RESFire) model in the Community Earth System Model (CESM) that provides modeling capability to reproduce the observed burning patterns and trends and to understand fire related climatic processes. Comparing with the default Community Land Model version 4.5 fire model in CESM, the RESFire model includes heterogeneous natural and anthropogenic constraints on fire ignition and spread, improved fire impact parameterization including online fire emissions and fire induced land cover changes, and modeling bias corrections for online fire weather simulation. Evaluation results based on the International Land Model Benchmarking package show significant improvements in fire simulation performance. The overall modeling score of burned area simulation increases from 0.50 with Community Land Model version 4.5 to 0.62 (RESFire driven by the observation-reanalysis data) and 0.60 (RESFire driven by the bias-corrected Community Atmosphere Model version 5 simulation). The attribution analysis of decadal burned area trends suggests distinct contributions of natural and anthropogenic forcing in different regions, which are consistent with previous observations. The model also includes a fire impact module for estimating atmospheric responses to fire emissions as well as fire disturbances on ecosystems, land cover, and surface radiation budget. These results demonstrate the latest progress of global fire model development that enables fully interactive climate-fire-ecosystem studies using CESM.

Plain Language Summary We improved the fire simulation capability in the Earth system model to better understand the complex interactions among climate, fire, and ecosystems with anthropogenic disturbance.

1. Introduction

Fires are a widespread phenomenon around the world and have a long history of interactions with climate, ecosystems, and human society (Bowman et al., 2009). Global fire activities are strongly influenced by four key factors: fuel availability, fire weather, ignition agents, and human activities (Flannigan et al., 2009), and fires exert profound feedback to earth systems through direct energy fluxes and large amounts of greenhouse gas (GHG) and aerosol emissions as well as disturbances on biogeochemical and hydrological cycles (Bowman et al., 2009). These interactions occur at multiple spatial and temporal scales that increase the difficulty to model fires in climate models. At short term and regional scales, local weather changes modulate burning frequency and intensity through lightning ignition and drought enhancement, while vegetation distributions determine fuel availability and combustibility. In a recent study, Veraverbeke et al. (2017) identified lightning as a major drive of large fires in North American boreal forests and found increasing trends of lightning ignitions in the past four decades and future projections. In Africa, opposite burning trends over southern and northern Africa were attributed to precipitation changes driven by the transition from El Niño to La Niña over the study period (Andela & van der Werf, 2014). Such meteorological and hydrological influences on fires were also found in other fire-prone regions including Southeast Asia (Field et al., 2016)

and South America (Chen et al., 2011). Meanwhile, fires concurrently impose feedback to both weather and ecosystems by releasing large amounts of gaseous and particulate emissions as well as heat, perturbing atmospheric chemical and thermodynamic processes and radiative forcing, and reshaping vegetation structure, composition, and distributions (Heilman et al., 2014; Liu et al., 2014). For instance, fire aerosols could affect clouds and precipitation in a nonlinear manner with initially suppressed but ultimately invigorated precipitation due to high smoke loadings (Lu & Sokolik, 2013). Fires also reshape local ecosystems by inducing vegetation mortality and restoration (Brando et al., 2014; Keeley, 2009) and further disturb regional to global carbon balance (Gatti et al., 2014). In fire seasons, large wildfires usually result in severe air pollution and pose a high risk to public health and human society (Johnston et al., 2012; Knorr et al., 2017; Marlier et al., 2013).

At longer timescales and larger spatial scales, these fire-climate interactions shift fire regimes in response to changes in the climate system and ecosystems affecting biogeochemical cycles, land cover, and hydrological cycles (Liu et al., 2014). Paleoclimate records indicated clear links between fire activities and abrupt climate change in North America during the last glacial-interglacial transition period (Marlon et al., 2009). Several observational and modeling studies also showed the occurrence of shifting fire regimes in many regions such as increasing large wildfires over the western United States due to the changing climate in the past centuries (Westerling et al., 2006; Yang et al., 2015). Besides climatic drivers, fires are also affected by human activities in terms of fire ignition and suppression (Archibald et al., 2012; Bowman et al., 2011). A fire history study suggested shifting driving force of the global fire regime from precipitation driven during the preindustrial period to human driven after the Industrial Revolution, and then to a temperature-driven global fire regime in future projections (Pechony & Shindell, 2010). This finding was corroborated by several other studies (Andela et al., 2017; Yang et al., 2014) that attributed the declining trend of global burned areas in the last century to human activities such as agricultural expansion and intensification, especially in tropical savanna regions. In return, fires not only contribute directly to the climate system by releasing large amounts of GHG and carbonaceous aerosol emissions but also disturb the radiation budget by changing surface albedo via aerosol deposition and postfire succession. Currently, several global fire emission data sets have been developed using different methods based on satellite retrievals (Ichoku & Ellison, 2014; Kaiser et al., 2012; Randerson et al., 2012; van der Werf et al., 2010, 2017). Though the differences among these emission estimations are large due to uncertainties in emission factors and the lack of satellite sensitivity to small fires (Randerson et al., 2012), biomass burning is still considered as one of the largest sources contributing to global warming over both short (20-year) and long (100-year) timescales for 1-year pulse fire emissions (Myhre et al., 2013). However, it is worth noting that this modeling result is based only on the radiative effects of source-specific GHGs and aerosol-radiation interactions without considering fire-climate-ecosystem feedbacks and aerosol-cloud interactions. Biomass burning could be carbon neutral with fire-induced CO_2 emissions being balanced by uptake from surviving and regenerating vegetation when climate and fire regimes reach equilibrium at a long-term scale (Bowman et al., 2009). It is also reported that the net effect of biomass burning would change from increasing radiative forcing in the burning year to decreasing radiative forcing over a long-term (80-year) fire cycle due to multidecadal increases of surface albedo as observed in boreal forests (Randerson et al., 2006) and simulated in other biomes (Ward et al., 2012).

To understand these complex climate-fire-ecosystem interactions, multiple fire models have been developed in the past few decades. The modeling complexity increases from simple statistical models with empirical algorithms to advanced process-based parameterizations coupled with terrestrial ecosystem models (TEMs) and dynamic global vegetation models (DGVMs). Statistical models based on empirical relationships between contemporary climate and fuel conditions and fire characteristics are developed to investigate climatic drivers of fires (Chen et al., 2011) and to examine future fire projections (Yue et al., 2013). Process-based models are usually implemented in TEMs and DGVMs to explicitly simulate fire-related processes including ignition, spread, and impacts. Hantson et al. (2016) summarized global fire modeling development history and reviewed the current status of multiple process-based fire models in the Fire Model Intercomparison Project that was initialized in 2014. One common problem with the current generation of fire models discussed by Hantson et al. (2016) is the simply represented fire effects on ecosystem dynamics and land use changes (Running, 2008). Current process-based fire models share more similarity in fire impact simulation than the other aspects given the simple treatment of fuel combustion, tree mortality, and postfire regeneration. The MC-FIRE model (Lenihan et al., 1998; Lenihan & Bachelet, 2015) and the LPJ-SPITFIRE model (Thonicke et al., 2010) have more explicit tree mortality simulation with

consideration of fire intensity and residence time. The LPX-Mv1 model (Kelley et al., 2014), which simulates resprouting after fires, is the only fire model in the Fire Model Intercomparison Project study with some modeling capability to explicitly simulate fire-triggered ecosystem regeneration processes. Though fire ignition and spread are relatively better represented than fire impacts, the fire models have limited modeling capacity to simulate diversified fire regime characteristics at regional scales (Hantson et al., 2016). Fire models are unable to reproduce observed burned area trends in specific regions like African savannas that are driven by both regional climate changes and demographic and socioeconomic impacts (Andela et al., 2017; Andela & van der Werf, 2014). Such limitations are due in part to the use of homogenous fire parameterization at coarse spatial and temporal scales that do not account for regional differences of fire behavior and characteristics (Rogers et al., 2015). Moreover, most fire models mainly consider one-way perturbations from weather to fires with incomplete feedback mechanisms from fires to weather and climate systems, and fire assessment studies usually use fixed fire emissions without consideration of fire feedbacks (Ward et al., 2012). The two-way interactions between climate and fires are indispensable in fire-related climate research and fire impact assessments. These interactions occur from the flame front to larger scales need to be incorporated into climate models to capture the climate effects on fire regimes as well as fire feedbacks to the atmosphere (Bowman et al., 2009). Terrestrial ecosystems would also change greatly with at least a doubling of forests in the flammable savanna regions in the absence of fire impacts (Bond et al., 2005).

In this paper, we developed a REgion-Specific ecosystem feedback fire (RESFire) model coupled in the land model (the Community Land Model version 4.5 [CLM4.5]) and the atmosphere model (the Community Atmosphere Model version 5 [CAM5]) of the Community Earth System Model (CESM) to extend the fire modeling capability. RESFire is capable of simulating the interactions of fires with climate and ecosystems within the framework of an earth system model. The major features in RESFire include (1) region- and vegetation-specific representation of natural forcing and demographic influences on fire occurrence and spread; (2) online calculation of fire emissions of mass (tracer gases and aerosols) and energy (sensible and latent heat) fluxes coupled between the land and atmosphere models; (3) incorporation of fire effects on ecosystems such as vegetation mortality, regrowth, and associated land cover changes; and (4) atmospheric model bias corrections to ensure the modeling performance consistency between online coupled climate simulations and offline simulations driven by atmospheric reanalysis and observation data. Given the broad scope and content of the model development and evaluation processes, we mainly focused on fire occurrence, spread, and impacts on terrestrial ecosystems in this paper. Although fire plume rise parameterization is also a part of the RESFire development, it will be described in a subsequent paper (currently in preparation) including modeling and parameterization details and evaluation. All the model variables used in this work are listed in Table S1 in the supporting information.

2. RESFire Model Description and Simulation

2.1. The Community Earth System Model

CESM is a fully coupled global climate model maintained by the National Center for Atmospheric Research (Hurrell et al., 2013). It is composed of five major components of the earth system including atmosphere, land surface, ocean, sea ice, and land ice, plus one central coupler component. As the final release of the CESM1 series, CESM version 1.2.2 has numerous new key features to improve modeling and prediction capability of the climate system. We developed the RESFire model in the CLM4.5 land model (Oleson et al., 2013) of CESM version 1.2.2 that supports both a stand-alone mode with only land model activated and a two-way coupled mode with dynamic land and atmosphere models. The spatial resolution we use is 0.9° (lat) × 1.25° (lon) with a time step of 30 min. In this study, the stand-alone CLM4.5 was driven by the combination of atmosphere observations and reanalysis data from 1991 to 2010 provided by the Climatic Research Unit and National Centers for Environmental Prediction (CRUNCEP; Viovy, 2013), while the two-way coupled CLM4.5 was driven by the CAM5 atmosphere model (Neale et al., 2012). RESFire was coupled in CLM4.5 in both simulation modes and additional interfaces between CLM4.5 and CAM5 were implemented for fire-related mass and energy fluxes in the two-way coupled mode. These newly incorporated fire modeling features are compatible with multiple major improvements in both CAM5 and CLM4.5 such as a new 3-mode modal aerosol scheme, a prognostic two-moment cloud formulation, and a revised photosynthesis scheme (Neale et al., 2012; Oleson et al., 2013), which help the simulation and evaluation of fire-atmosphere-vegetation interactions such as fire aerosol radiative effects and carbon
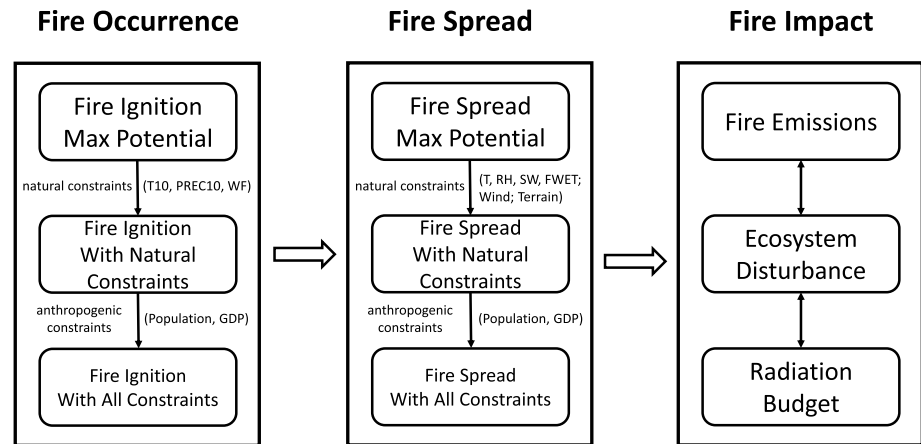
Fire Occurrence　　**Fire Spread**　　**Fire Impact**

Figure 1. A schematic diagram of the RESFire model development (please see Tables 3 and 4 for fire weather variable description). RESFire = REgion-Specific ecosystem feedback Fire; T10 = surface temperature; PREC10 = precipitation; WF = soil moisture; RH = relative humidity; GDP = gross domestic production; SW = surface soil wetness; FWET = fraction of wet canopy.

budget disturbance. Thereby, RESFire provides the state-of-the-science simulation capability to examine the physical, chemical, and biogeochemical processes through which fires interact with climate and terrestrial ecosystems.

2.2. RESFire Model Framework

To account for climate-fire interactive processes comprehensively, RESFire in CESM includes three major components (Figure 1): fire occurrence estimation, fire spread optimization, and fire impact parameterization (Li et al., 2012, 2013; Thonicke et al., 2010). We started from the maximum fire count estimation, which was considered as the maximum fire occurrence potential triggered by both natural and anthropogenic ignitions. Then we added natural constraints on the maximum fire occurrence potential to estimate fire counts with consideration of fire weather impacts. We further added anthropogenic constraints on fire counts to generate final fire count estimation with complete natural and demographic influence. The final fire count product in combination with fire spread parameterization was used for burned area estimation at the next step. The maximum fire spread potential for a single fire spot in one grid cell was estimated by multiplying maximum fire spread rates with an average fire duration time using an elliptical fire spread shape assumption. This assumption was proposed by van Wagner (1969) and adopted by many process-based fire models (Albini, 1976; FCFDG, 1992; Li et al., 2012; Thonicke et al., 2010). We added natural and anthropogenic constraints sequentially on the maximum fire spread potential to optimize burned area estimation. The optimized burned area estimation was used lastly in fire impact parameterization. In RESFire, fire impacts consist of direct mass and energy fluxes that are exchanged between land surface and atmosphere as well as fire disturbance on ecosystems such as fire induced tree mortality and associated recovery processes. These ecosystem changes could further lead to indirect fire impacts on the climate system by perturbing hydrological cycle, radiation budget due to surface albedo changes, and terrestrial ecosystem productivity.

To represent distinct fire characteristics for different vegetation types and regional climate and socioeconomic conditions, we divided the global land areas into eight subregions (Table 1; Figure 2a) and included the plant functional types (PFTs) into five major groups (Table 2; Figure 2b). It reflects a balance between representing fire regime diversity and reducing model complexity. We assumed that the dependence of fires on PFT types is much more homogeneous within a region than between different regions. The eight geographical regions were combined from the 14 Global Fire Emissions Database (GFED) subregions (Giglio et al., 2010) to represent (1) the continuity of PFT distributions within a region and (2) different latitudinal and climate zones. We then developed region- and PFT-specific fire parameterizations for biomes in these subregions to improve the RESFire modeling capability. Such region- and PFT-specific parameterizations were applied in the three major RESFire components (Figure 1) to account for regional and biome diversities in fire behavior, socioeconomic effects, and climate impacts.

Table 1
Regions Used in the RESFire Model

Region	Abbreviation	Full name
R1	NTHA	North America
R2	STHA	South America
R3	EURA	Eurasia excluding Middle East and South Asia
R4	MENA	Middle East and North Africa
R5	NHAF	Northern Hemisphere Africa
R6	SHAF	Southern Hemisphere Africa
R7	SSEA	South and Southeast Asia
R8	OCEA	Oceania

Note. RESFire = REgion-Specific ecosystem feedback Fire.

2.3. Fire Occurrence

Fire can be triggered by either natural or anthropogenic ignitions. The maximum fire ignition potential N_{clm}^0 (count per grid cell per time step) in RESFire is given in equation (1),

$$N_{clm}^0 = (I_n + I_a)A_g, \tag{1}$$

where I_n and I_a are the numbers of maximum fire ignition (count per square kilometer per time step) triggered by natural and anthropogenic sources, respectively, and A_g is the grid cell area (square kilometer per grid cell).

The natural fire ignition is a function of the cloud-to-ground fraction of lightning flashes I_l (flash per square kilometer per time step) and latitude λ (°) (Li et al., 2012; Prentice & Mackerras, 1977),

$$I_n = \frac{1}{5.16 + 2.16\cos(3\lambda)}I_l, \tag{2}$$

and the anthropogenic fire ignition is a function of population density D_p (person per square kilometer; Pechony & Shindell, 2009; Venevsky et al., 2002;),

$$I_a = \frac{\alpha D_p 6.8 D_p^{-0.6}}{n}, \tag{3}$$

where $\alpha = 3.89 \times 10^{-3}$ (count per person per month) is the number of potential ignition by a person per month, and n is the number of time steps per month (time step per month).

The fire ignition potential N_{clm}^0 is considered as the maximum fire spot number estimation without any fire weather influence. It does not take into account the diversity of fire related socioeconomic conditions or variable fire management capability among different regions either. Therefore, we next conducted the observation-based regression analysis to incorporate both natural and anthropogenic constraint relationships into the fire model.

2.3.1. Natural Constraints on Fire Occurrence

On top of the maximum fire ignition potential, we added region- and PFT-specific natural and anthropogenic constraints sequentially to represent enhancement and suppression effects on fire activities on a regional basis. The natural constraint factors consist of three fire weather variables: surface temperature (T10, K), precipitation (PREC10, mm/s), and soil moisture (WF, %; Table 3; Flannigan et al., 2009). The first two meteorological variables were used by several drought indices to characterize the atmosphere and hydrological drought conditions (Keyantash & Dracup, 2002). In our fire model, we considered these drought-related variables in a continuous time window (10-day running mean) to better represent the probability
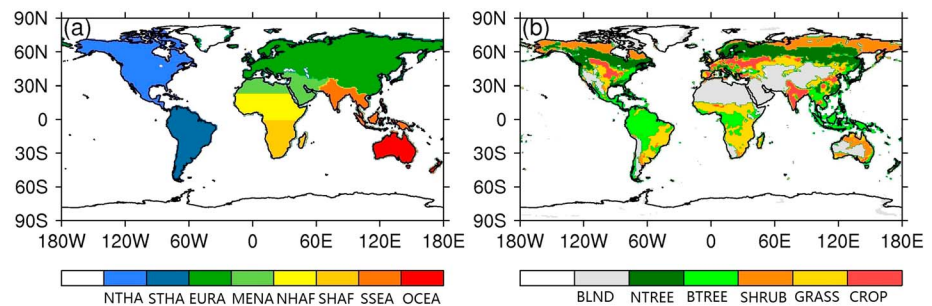

Figure 2. Geographical regions (a) and dominant plant functional type (PFT) groups (b) used by the region- and PFT-specific region-specific ecosystem feedback fire model. Each Community Land Model grid has multiple PFT types at subgrid level. Only dominant PFT types with the largest fractions are shown in (b). The acronyms of region and PFT are listed in Tables 1 and 2, respectively.

Table 2
PFT Groups Used in the RESFire Model

PFT groups	Abbreviation	Full name
—	BLND	Bare land
P1	NTREE	Needleleaf tree
P2	BTREE	Broadleaf tree
P3	SHRUB	Shrub
P4	GRASS	Grass
P5	CROP	Crop

Note. RESFire = REgion-Specific ecosystem feedback Fire; PFT = plant functional type.

of fire occurrence as a consequence of cumulative effects in ambient environonment and fuel conditions. The last hydrological variable was used by a previous study (Li et al., 2012) to characterize fuel combustibility. For training purposes in the regression analysis, we obtained monthly fire weather data from the CRUNCEP observation-reanalysis product. We then used the observation-reanalysis combined weather data and satellite observed fire count data to train the regression model. Before building models, we rescaled and interpolated most original training input data such as the fire weather reanalysis data in Tables 3 and 4 to the same scales of our modeling outputs, which are monthly-based gridded results at the 0.9° (lat) × 1.25° (lon) resolution. We then developed the constraint regression models between these inputs and outputs and implemented the statistical relationships into our fire model. We did similar processing for bias corrections in section 2.6, except that the training data changed to the daily-based reanalysis and model data so that we had more samples for distribution mapping.

The omission of any fire weather impact or socioeconomic effect in N_{clm}^0 leads to large discrepancies between the maximum fire ignition potential and observed fire counts. We then defined a common logarithm-based natural scaling factor NS_n (unitless) for fire count estimation in equation (4),

$$NS_n = \log_{10}\left(N_{modis}/N_{clm}^0\right), \tag{4}$$

where N_{modis} (count per grid cell per time step) is satellite observed fire counts that are interpolated from the monthly Moderate Resolution Imaging Spectroradiometer (MODIS) climate modeling grid fire count product (MYD14CMH) on board of the EOS-Aqua platform (Giglio et al., 2006). It is noted that the original MODIS climate modeling grid fire product is generated at a 0.5° spatial resolution from 1-km pixel level active fire products with cloud cover corrections. This MODIS product provides an approximate estimation for actual fire numbers with an implicit assumption that every fire pixel is derived from an actual fire spot and is independent from any other. Although the satellite data may be biased due to duplication or missing count, no other data sets provide the temporospatial coverage of these data. As a result, this product was widely used for fire count assessments in previous modeling studies (Li et al., 2012; Thonicke et al., 2010). Hantson et al. (2013) discussed the strengths and weaknesses of using MODIS active fire products to characterize global fire occurrence and found variable relations between MODIS fire spots and burned area in space and time. Such complex relationships underline the necessity for region-specific parameterization in our work. We interpolated the MODIS data to the modeling grid and used 4 years of the monthly MODIS data (2003–2006) to investigate the natural constraint relationship. We chose the 4 years from 2003 to 2006 since there were relatively small interannual variability in both major climate modes and global fire activities. Therefore, we could focus on seasonal variations by using data of nonextreme years for model training and test the modeling predictability of extreme years.

We examined the region-specific relationship between NS_n and fire weather factors using multilinear ridge regression models for each subregion (equation (5)),

$$NS_n^{i,j} = \sum_{k=1}^3 \beta_k^{i,j} \cdot X_k, \tag{5}$$

Table 3
Fire Weather Factors Used as Natural Constraints on Fire Occurrence

Fire weather factors	Units	Description
T10[a]	K	10-day running mean of 2-m temperature
PREC10[a]	mm/s	10-day running mean of total precipitation
WF[b]	%	Soil water fraction for top 0.05-m layers

Note. T10 = surface temperature; PREC10 = precipitation; WF = soil moisture.
[a]Meteorological variables to depict drought conditions (Keyantash & Dracup, 2002).   [b]A hydrological variable to characterize fuel combustibility (Li et al., 2012).

where X_k is the three spatial and temporal variable fire weather factors in Table 3 and $\beta_k^{i,j}$ is the corresponding regression coefficient of the kth factor associated with the ith PFT group in the jth subregion. $NS_n^{i,j}$ is obtained by filtering out gridded NS_n in the jth subregion with the fraction of the ith PFT group greater than 30% in the monthly observational data from 2003 to 2006. To separate the temporal and spatial variations in the relationship, we trained the regression models with spatially averaged and temporal-averaged data, respectively. Specifically, we first regionally averaged the monthly fire weather factors $X_k(x, y, t)$ and the corresponding $NS_n^{i,j}(x, y, t)$ in the jth subregion with gridded observational burned area

Table 4
Fire Weather Factors Used as Natural Constraints on Fire Spread

Fire weather factors	Units	Description
TBOT[a,b]	K	Surface air temperature
RH[a,b]	%	Surface air relative humidity
SW[b,c]	Unitless	Surface soil wetness factor
FWET[c]	%	Fraction of wet canopy

Note. TBOT = surface air temperature; RH = relative humidity; SW = surface soil wetness; FWET = fraction of wet canopy. [a]Meteorological variables to control the short-term moisture content of fuels. [b]Li et al. (2012). [c]Hydrological variables to characterize both the short-term and long-term moisture content of fuels.

as averaging weights. We used weighted averaging to highlight major burning areas vulnerable to fires. Therefore, we generated monthly time series of fire weather factors $\overline{X}_k(t)$ and natural scaling factors $\overline{NS}_n^{i,j}(t)$ for each subregion and then estimated the regression coefficients $\overline{\beta}_k^{i,j}$ using ridge regression for temporal variations. Similarly, we regressed annually averaged $\widetilde{NS}_n^{i,j}(x,y)$ on annual mean weather factors $\widetilde{X}_k(x,y)$ (all with monthly burned area as averaging weights) and estimated the regression coefficients $\widetilde{\beta}_k^{i,j}$ using ridge regression for spatial distributions. We applied the average of $\overline{\beta}_k^{i,j}$ and $\widetilde{\beta}_k^{i,j}$ in the RESFire model to capture the spatial and temporal variability simultaneously and set the constant term $\beta_0^{i,j}$ as the regional annual mean deviation between observed $NS_n^{i,j}$ and simulated $\widehat{NS}_n^{i,j}$ (equation (6)),

$$\widehat{NS_n^{i,j}} = \sum_{k=1}^3 \frac{\left(\overline{\beta}_k^{i,j} + \widetilde{\beta}_k^{i,j}\right)}{2} \cdot X_k(x,y,t) + \beta_0^{i,j}. \tag{6}$$

It is worth noting that we conducted variable selection first to reduce collinearity problems in the regression model. If the correlation between two input variables exceeded a threshold, we removed one of them and built the regression model with the rest of input variables. In this way, the coefficient estimates are more robust with less erratic changes in response to variations in the modeling data. Furthermore, the ridge regression method, which is a penalized regression method, has low sensitivity to collinearity and shows great potential to reduce the negative impact of the collinearity problem in ecological studies (Dormann et al., 2013). We set the threshold value at 0.7 as suggested by Dormann et al. (2013) for correlations among the predictor variables. When two predictor variables showed $|r| > 0.7$, we excluded the variable that had less correlation to the dependent variable ($NS_n^{i,j}$ in equation (6)) in the regression model.

Figure 3 illustrates the temporal variability of fire occurrence in both observation and regression-estimated data for each region and PFT group. Since cropland fires are mostly controlled by agricultural activities with strong anthropogenic influence on the seasonality and spatial distributions (Magi et al., 2012; Zeng et al., 2008), we parameterized cropland fires separately by focusing on socioeconomic factors following previous studies (Li et al., 2013). Therefore, we only applied natural and anthropogenic constraints to the PFT groups 1–4 (Table 2). Generally, most of regression-estimated data reproduce the seasonality in the observational data for different PFT groups in each region, which are reflected by relatively high correlation coefficients between regression-estimated and observed data on the top of each subplot (for instance, $r = 0.97$ for PFT group 4 in region 5; Figure 3 [P4R5]). African regions (R5-6) show the strongest burning seasonality for all PFT groups, with peak fire seasons in cold and dry months in both Northern and Southern Hemispheres of Africa. The temporal regression models capture well these seasonal changes by showing good agreement of regression-estimated data with the observations. The spatial variation models capture the spatially heterogeneous burning distributions in a similar manner, though the spatial predictability (Figure S1) is not as high as the temporal predictability due to larger spatial variability in fire occurrence.

2.3.2. Anthropogenic Constraints on Fire Occurrence

We defined a demographic scaling factor for fire count (AS_n, unitless) in the same manner of NS_n after including natural constraints:

$$AS_n = \log_{10}\left(N_{modis}/N'_{clm}\right), \tag{7}$$

where N'_{clm} is the intermediate fire count estimation (count per grid cell per time step) with consideration of only natural constraints NC_n (unitless):

$$N'_{clm} = N^0_{clm} \times NC_n. \tag{8}$$

The natural constraint NC_n in the jth subregion is a weighted average of exponents of scaling factors NS_n for the ith PFT group with the weight of its fractional coverage f^i (%):
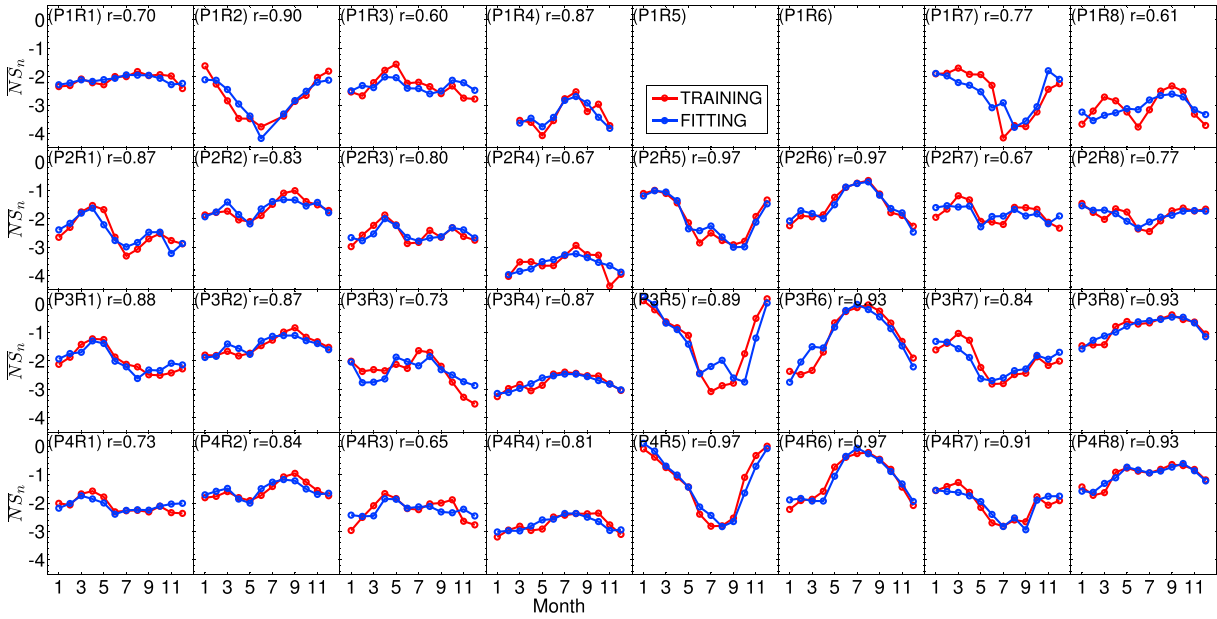
Figure 3. Region- and plant functional type (PFT)-specific (see Tables 1 and 2 for the full names of regions and PFT numbers shown on the top left corners) natural constraints on the temporal variations of fire occurrences. The temporal correlation coefficients between observed and regression-estimated data for each PFT group and region are shown next to the subplot titles.

$$NC_n = \sum_{i=1}^{n} \left(10^{NS_n^{i,j}} \times f^i \right). \tag{9}$$

Given the large variations and uncertainties of the raw data, we followed the method of Li et al. (2013) and resampled the data by averaging AS_n in 50 consecutive bins of population density in the log scale and then generated linear and nonlinear weighted fitting functions by setting sampling sizes as weights for the resampled data in each bin. We obtained anthropogenic constraints for the four PFT groups in the eight subregions based on these weighted fitting functions between population and anthropogenic scaling factors (Figure 4). The anthropogenic constraint relationships vary among different PFT groups and regions. For instance, Eurasia (R3) as the most populated region generally shows a strong human suppression effect for most PFT groups because of effective early detection and prevention of fire danger. On the contrary, South America (R2) demonstrates predominant enhancement effects for many PFT groups, especially in less-populated regions, which could be related to deforestation burning activities over these regions. In North America (R1), the distinctions between prescribed burning in the Southeast United States and large wildfires in the western United States lead to more complex nonlinear relationships with mixed suppression and enhancement effects for many PFT groups.

We estimated anthropogenic constraints AC_n (unitless) based on anthropogenic scaling factors and PFT fractional coverages in the same manner as the natural constraints NC_n,

$$AC_n = \sum_{i=1}^{n} \left(10^{AS_n^{i,j}} \times f^i \right), \tag{10}$$

where $AS_n^{i,j} = f\left(D_p\right)$ is a weighted fitting function of population density as shown in Figure 4.

After taking into account both natural constraints NC_n and anthropogenic constraints AC_n, we estimated the final fire count estimation N_{clm}^f (count per grid cell per time step) in equation (11):

$$N_{clm}^f = N_{clm}^{'} \times AC_n = N_{clm}^0 \times NC_n \times AC_n. \tag{11}$$

This final fire count estimation is the basis for burned area and fire impact parameterization in the following sections.
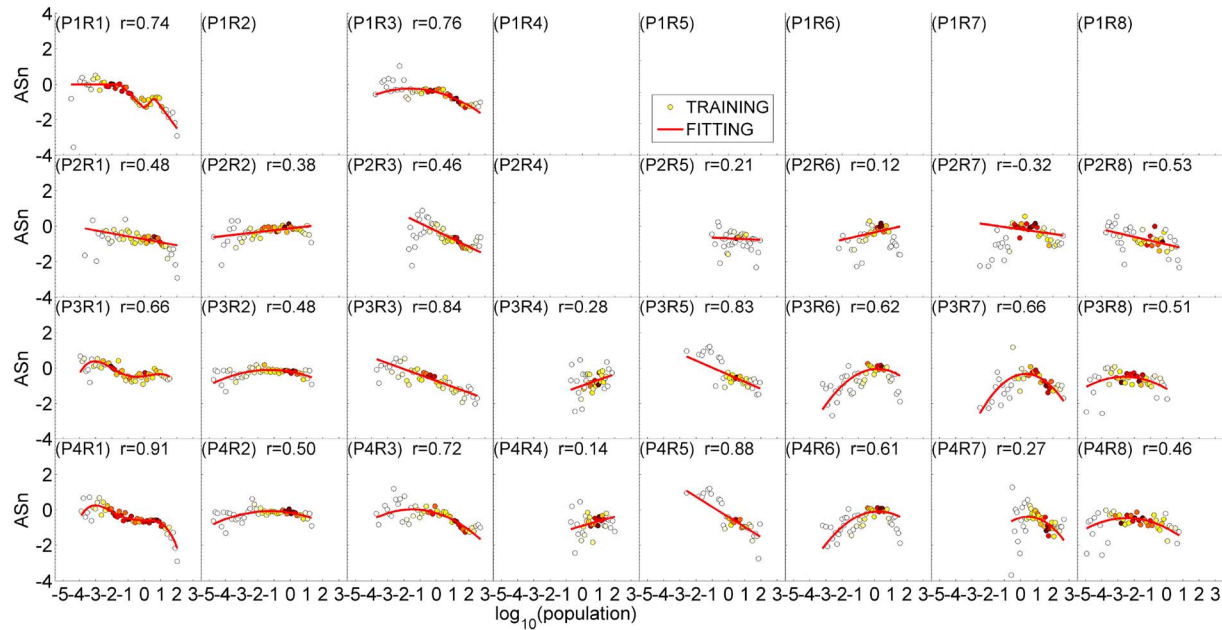
Figure 4. Same as Figure 3 but for anthropogenic constraints on spatial variations of fire occurrence; the color saturation in each circle denotes the density of sampled grid cells in each bin of population density. See detailed explanation in the main text.

2.4. Fire Spread

To simulate burned area in the fire model, we need to estimate fire spread in addition to fire occurrence. We generated the maximum potential of gridded burned area fractions (BA^0_{clm}, percent per time step) as a function of fire count (N^f_{clm}, count per grid cell per time step) and maximum spread area fraction per fire spot (A_{max}, percent per grid cell per count):

$$BA^0_{clm} = N^f_{clm} \times A_{max}. \tag{12}$$

The maximum spread area per fire spot (A_{max}) was parameterized using the assumption of an elliptical spreading shape (Albini, 1976; FCFDG, 1992; Li et al., 2012; Thonicke et al., 2010; van Wagner, 1969) and passive suppression due to terrain impedance and landscape fragmentation (Pfeiffer et al., 2013). Specifically, the elliptical fire spreading area A^{ellip}_{max} is a function of PFT-dependent maximum fire spread rates (fsr_{max}, m/s), average fire duration time (τ, s), length-to-breath ratio ($L_B = 1.0 + 10.0[1 - \exp(-0.06W)]$, where W is wind speed with the unit of m/s; L_B is unitless), and head-to-back ratio of the theoretical elliptical fire shape ($H_B = \frac{L_B + (L_B^2 - 1)^{0.5}}{L_B - (L_B^2 - 1)^{0.5}}$, unitless) in equation (13) adopted from Li et al. (2012):

$$A^{ellip}_{max} = \frac{\pi \times \left(fsr_{max} \times \frac{0.1 L_B}{1 + \frac{1}{H_B}} \right)^2 \times \tau^2}{4 \times L_B \times A_g} \left(1 + \frac{1}{H_B} \right)^2 \times 10^{-6}. \tag{13}$$

We set the average fire duration time (τ) to 24 hr following previous fire modeling studies (Arora & Boer, 2005; Kloster et al., 2010; Li et al., 2012). The passive fire suppression due to terrain impedance was adopted from Pfeiffer et al. (2013), which represents the scarcity of larger fires in mountain regions. The terrain impedance factor (slf, unitless) was determined in equation (14) as a piecewise function of median terrain slope angle (γ, °), which limits the impedance effect only in grid cells with a median slope angle larger than $1.7°$. We calculated the grid median slope angle γ following the method by Zhang et al. (1999) method to aggregate the maximum eight-direction (D8) slope at 1-arc minute resolution based on the ETOPO1 global digital elevation model (Amante & Eakins, 2009) in equation (14):

$$slf = \begin{cases} 1 & \gamma < 1.7^{\circ} \\ \dfrac{1}{\frac{5}{9}\pi\gamma - 2} & \gamma \geq 1.7^{\circ} \end{cases}. \tag{14}$$

Similarly, we adopted the landscape fragmentation suppression factor (A_{max}^{frag}, percent per grid cell per count) from Pfeiffer et al. (2013) in equation (15):

$$A_{max}^{frag} = \left(1.003 + e^{(16.607 - 41.503 f^{non-crop})}\right)^{-2.169}, \tag{15}$$

which is approximated as a function of noncrop PFT fractions in grid cells ($f^{non-crop}$, percent per grid cell) based on the Monte Carlo simulation results.

The fragmentation suppression factor is the average contiguous area fraction of natural PFT patches in each grid cell, which sets the upper limit of burned area fraction of individual fire spots in equation (16):

$$A_{max} = \min\left(A_{max}^{frag}, slf \times A_{max}^{ellip}\right). \tag{16}$$

We then defined a logarithm-based natural scaling factor for fire spread (NS_a, unitless) based on the ratio of the GFED burned area product and simulated maximum fractional burned area potential in equation (17):

$$NS_a = \log_{10}\left(\frac{BA_{GFED}}{BA_{clm}^0}\right), \tag{17}$$

where BA_{GFED} (percent per time step) is the satellite based GFED4.1s burned area estimation with contributions from small fires (Giglio et al., 2013; Randerson et al., 2012; van der Werf et al., 2017). We interpolated the GFED4.1s burned area to the modeling grid and time step to evaluate the parameterization.

2.4.1. Natural Constraints on Fire Spread

In burning events, fire spread is constrained mostly by wind and fuel combustibility, the latter of which is a function of moisture content of the fuel bed. Since we already accounted for the wind factor in the elliptical fire spreading area $\left(A_{max}^{ellip}\right)$, here we used surface air temperature (TBOT, K), relative humidity (RH, %), surface soil wetness (SW, unitless), and the fraction of wet canopy (FWET, %) as surrogates to characterize fuel combustibility (Table 4). The first two meteorological factors, TBOT and RH, affect the transfer of water vapor into and out of fine fuel and the short-term fuel moisture content. The last two hydrological factors, SW and FWET, result from the accumulated effects of rainfall that modulate the fuel moisture content and affect fire behavior at both short-term (hourly) and long-term (seasonal) timescales.

We applied natural constraints on fire spread calculation using the same equation (equation (5)) and parameterization processes of fire occurrence estimation. We conducted ridge regressions of NS_a on the four fire weather factors based on the 2003 to 2006 monthly observational data. Specifically, we first determined the collinear input variables using the threshold of 0.7 for correlation coefficients among independent variables. We then built two series of regression models for temporal and spatial variations of fire spread based on regional averaged and annual averaged regression data, respectively. Figure 5 shows region- and PFT-specific temporal variations of natural scaling factors in both observed and regression data. African regions (R5-6) again have the strongest seasonal variability of fire spread among all PFT groups. The fire spread seasonal variations in other biomes are less significant but nonnegligible, especially over the regions with strong weather seasonality. It is noted that fire seasonality could be variable among different PFT groups in the same region, such as the pronounced seasonal shift between peak fire months over the broadleaf forests (P2R8) and the grasslands (P4R8) in Australia. These differences are attributed to different climatic zones and fire regimes of the dominant biome. In Australia, broadleaf trees mostly grow in temperate zones of southeast Australia with the four-season pattern, while grass mostly grows in the tropical areas of northern Australia with the wet and dry climatic pattern just like the Southern Hemisphere of Africa (R6). These so-called "bushfires" tend to be most common and severe during summer and autumn (December–March) in forest areas because of higher temperatures and drought conditions that are conducive to fire spread, while bushfires in tropical savannas usually occur during the dry season (April–October) when the biomass is fully cured and ready to burn (Bradstock et al., 2012).
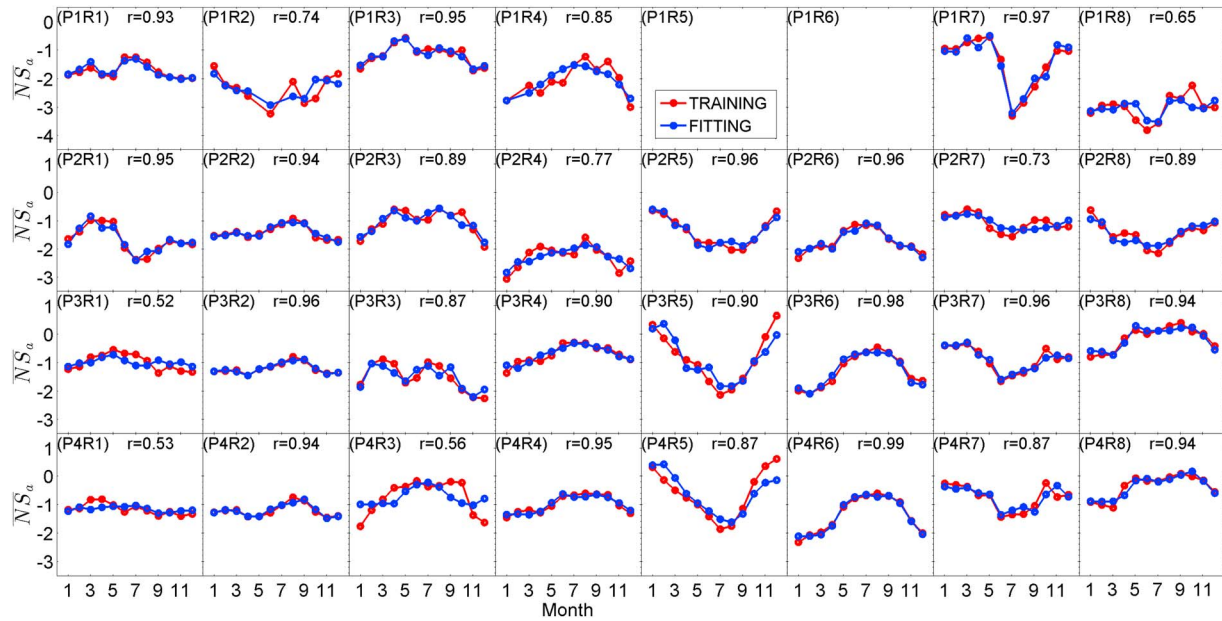
Figure 5. Same as Figure 3 but for fire spread.

Similar to fire occurrence, the regression parameterizations reproduce distinct seasonality characteristics of fire spread in different biomes. Figure S2 shows the regression-estimated results for spatial variations of natural influences on fire spread, which are significant in biomes such Africa and Australia savannas. Again, we estimated the natural constraint on burned area (NC_a, unitless) as weighted averaging of natural scaling factors NS_a for each PFT group and region (equation (18)):

$$NC_a = \sum_{i=1}^{n} \left(10^{NS_a^{i,j}} \times f^i \right). \tag{18}$$

After adding natural constraints on both temporal and spatial variations of fire spread, we next implemented anthropogenic impacts to finalize the fire spread parameterization.

2.4.2. Anthropogenic Constraints on Fire Spread

We defined a logarithm-based demographic scaling factor for fire spread (AS_a, unitless) to characterize human impacts on burned area:

$$AS_a = \log_{10} \left(\frac{BA_{GFED}}{BA'_{clm}} \right) = \log_{10} \left(\frac{BA_{GFED}}{BA_{clm}^0 \times NC_a} \right). \tag{19}$$

We applied equation (19) to all regions and PFT groups including cropland areas, where agricultural activities determine burning seasonality and crop residuals as fuel supply. It is noted that we only considered anthropogenic constraints on cropland fires and set NS_a for cropland fires to zero. NS_a for the other PFT fires were described in the previous section. We estimated the anthropogenic scaling factor AS_a in each biome by separately fitting polynomial functions with gridded population density distribution (Figure 6) and gross domestic production at country levels. Compared with anthropogenic constraints on fire ignition in Figure 4, Eurasia (R3) again shows suppression effects with increasing population density, though such effect is more significant in grasslands and cropland regions. South America (R2) has moderate fire enhancement effects with increasing population density over rain forest regions (P2). Such enhancements can be attributed to anthropogenic burning driven by deforestation and agriculture activities in this area. North America (R1) still shows mixed effects with both enhancement and suppression effects in many forest (P1/2) and cropland areas (P5), which might be related to the concurrence of prescribed burning and fire prevention practices in these areas. More varying demographic effects can be found in savannas of Africa with strong suppression effects in northern Africa (P4R5) and slightly enhancement effects in less-populated
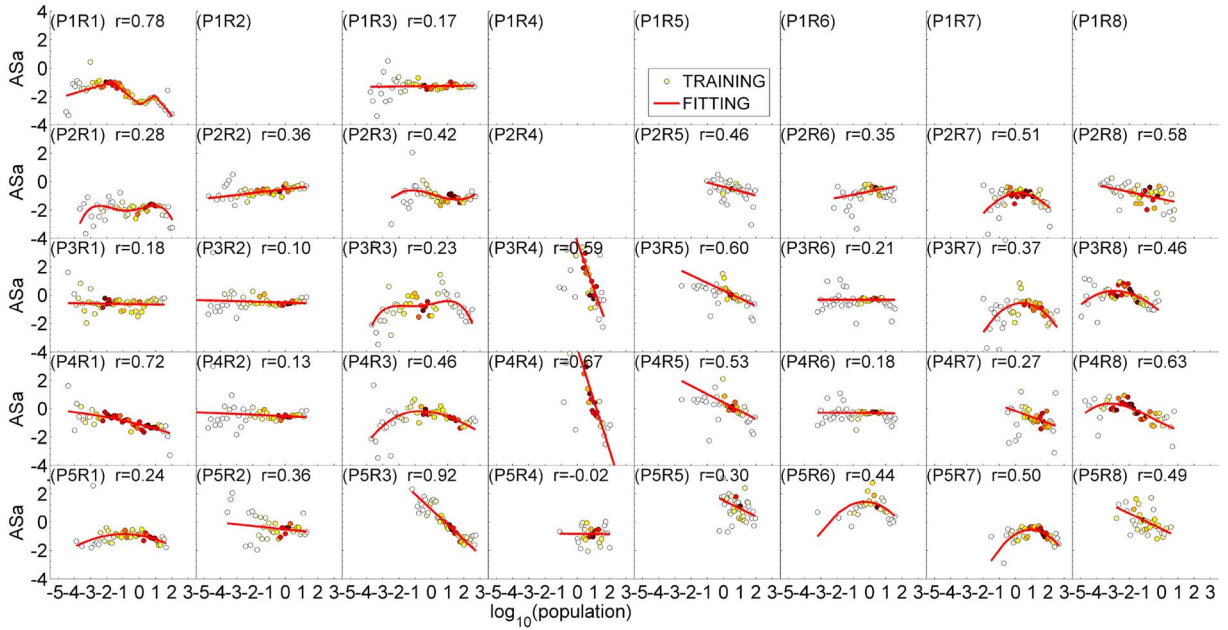
Figure 6. Same as Figure 4 but for the anthropogenic constraints on spatial variations of fire spread.

regions of southern Africa (P4R6). These relationships are consistent with an observation-based study (Andela et al., 2017) and will be discussed further in the following trend analysis.

With consideration of both natural and anthropogenic constraint effects, we estimated the final burned area fraction (BA_{clm}^{f}, percent per time step) using equation (20):

$$BA_{clm}^{f} = BA_{clm}^{0} \times NC_a \times AC_a, \tag{20}$$

where AC_a (unitless) is the anthropogenic constrain on burned area as weighted averaging of AS_a in equation (21).

$$AC_a = \sum_{i=1}^{n} \left(10^{AS_a^{i,j}} \times f^i \right) \tag{21}$$

2.5. Fire Impacts

We considered two types of fire impacts in the RESFire model: the short- and long-term effects. The short-term effect includes fire-related heat and mass release (flux rates) at hourly to weekly scales, and the long-term effect includes disturbances on ecosystems at much longer timescales such as postfire changes in land cover and ecosystem structure over decades due to fire-induced vegetation mortality (Li et al., 2014).

2.5.1. Fire Mass and Heat Fluxes

We estimated fire carbon emissions (E_{clm}^{c}, g C·m^{-2}·s^{-1}) as a combination of carbon stocks (C_i, g C/m^2), burned area fractions (BA_{clm}^{f}, percent per time step), a time unit conversion factor (Δt, second per time step), and PFT-specific combustion completeness (CC_i, unitless):

$$E_{clm}^{c} = \sum_{i=1}^{n} C_i \times \frac{BA_{clm}^{f}}{\Delta t} \times CC_i. \tag{22}$$

By multiplying corresponding emission factors, we estimated fire emissions in equation (23) for 39 tracer gases and aerosols (E_{clm}^{k}, g species per square meter per second) based on fire carbon emissions:

$$E_{clm}^k = \frac{E_{clm}^c}{cf^c} \times EF^k, \tag{23}$$

where $cf^c = 480$ (g C per kilogram per dry matter) is a carbon to dry matter conversion factor, and EF^k (g species per kilogram per dry matter) is the kth species' emission factor (Akagi et al., 2011) used by the GFED4.1s data.

We computed fire sensible heat flux as fire radiative power (FRP, W/m^2). We inversed the conversion factor cf^e (kilogram per dry matter per megajoule) used by Kaiser et al. (2012) to convert fire carbon emissions to sensible heat fluxes (E_{clm}^{SH}, MW/m^2):

$$E_{clm}^{SH} = \frac{E_{clm}^c}{cf^c \times cf^e}, \tag{24}$$

where cf^e are PFT-specific conversion factors ranging from 0.13 to 1.55 kg per dry matter per megajoule for nonpeat PFT groups (Table S2). The fire line intensity ($flint$, kW/m) was parameterized based on released fire energy and fire line length of the ellipse fire shape,

$$flint = \frac{E_{clm}^{SH}}{10^3 \times BA_f} \times fsr_{dw} \times \Delta t \times \frac{2 \times L_B}{\left(L_B + \sqrt{L_B^2 - 1}\right) \times \left(3 \times (L_B + 1) - \sqrt{3 \times L_B^2 + 10 \times L_B + 3}\right)}, \tag{25}$$

where fsr_{dw} is the fire spread rate (m/s) at downwind directions after considering natural constraints (equation (26)).

$$fsr_{dw} = fsr_{max} \times NC_a \times 0.05 \times \frac{2 \times L_B}{1 + \frac{1}{H_B}} \tag{26}$$

The fire-related moisture flux ($E_{clm}^{H_2O}$, g H$_2$O·m^{-2}·s^{-1}) was estimated based on stoichiometry by using equation (27) adopted from Jacobson (2014):

$$E_{clm}^{H_2O} = E_{clm}^c \times \frac{M_{H_2O}}{M_{CO_2}} \times cf^{H_2O}, \tag{27}$$

where $cf^{H_2O} = 0.83 \frac{mol\ H_2O}{mol\ CO_2}$ is the stoichiometry factor in the mass balance equation.

Finally, we obtained latent heat flux (E_{clm}^{LH}, W/m^2) by multiplying moisture flux with latent heat of evaporation (equation (28)):

$$E_{clm}^{LH} = E_{clm}^{H_2O} \times H \times 10^{-3} \tag{28}$$

with $=2.501 \times 10^6$ J/kg H$_2$O.

2.5.2. Ecosystem Effects

We considered both partial- and whole-plant mortality in the parameterization of fire related ecosystem effects. The partial-mortality parameterization is that of the default fire model in CLM (Li et al., 2012, 2013; hereafter indicated as LL2013) by transferring a part of unburned plant tissues (leaf, stem, root, etc.) to the litter pool with fixed tissue-mortality factors, while the whole-plant mortality is parameterized by multiplying simulated FRP with observation-based sensitivity relationships between plant mortality rates (MRs) and FRP. Though plant traits like bark thickness and tree sizes can also influence fire-induced tree mortality (Brando et al., 2012), such detailed information is unavailable in the CLM model used in this study because of its PFT-based modeling structure. More sophisticated parameterization can be developed with the "cohort"-based version of the CLM Ecosystem Demography model (Fisher et al., 2015) in the future. We collected multiple fire-induced plant MRs from field measurements and satellite observations for different PFTs (Table 5) and implemented the observation-based sensitivity relationships between tree mortality and fire intensity into the fire model. The whole-plant MRs are region- and PFT-dependent to reflect the nature of variable heat endurance of plant species to fire scorching. The newly incorporated whole-plant fire mortality and associated land cover changes are essential in climate-fire-ecosystem feedbacks (Cochrane et al., 1999).

Table 5
Fire-Induced Annualized Fractional Whole-Plant Mortality Rates for Each PFT Group

PFT	Mortality	Equations
Shrub	Fixed[a,b,c]	$MR = 30\,\%$, if $flint \geq 50$ kW/m
Broadleaf tree	$f(flint)$[d]	$MR = 0.000885 \times flint,\ flint \geq 0$
Needleleaf tree	$f(FRP)$[e]	$MR = \begin{cases} 0.0444 \times \log10(FRP) + 0.64,\ FRP>0,\ \text{North America} \\ 0.0783 \times \log10(FRP) + 0.26,\ FRP>0,\ \text{Eurasia} \end{cases}$

Note. PFT = plant functional type.
[a]Epting and Verbyla (2005). [b]Medeiros and Miranda (2008). [c]Richards and Lamont (1996). [d]Brando et al. (2014). [e]Rogers et al. (2015).

Table 5 lists the fire-induced whole-plant annualized fractional MRs (%) for each PFT except grasses and crops. Usually, grasslands can recover in a relatively short time period after burning due to reduced self-shading and competitive pressure (Zimmermann et al., 2010), and previous studies indicated positive feedback processes in the grass-fire cycle over many transitional forest edge and savanna regions (Balch et al., 2009; Bowman et al., 2014; Vila et al., 2001). For cropland, it is mainly constrained by agricultural practices instead of natural ecological succession. Therefore, we assumed less fire-induced perturbations in these two PFT groups than the others. There is no fire-induced land cover change for cropland in each grid cell, while grassland fractions can only vary passively as a consequence of shrub/tree coverage changes. For shrubs, we used the fixed whole-plant mortality of 30% once fire line intensity exceeded a threshold value of 50 kW/m based on the average of literature data (Epting & Verbyla, 2005; Medeiros & Miranda, 2008; Richards & Lamont, 1996). For broad leaf trees, the fire-induced whole-plant mortality was estimated as a linear function of fire line intensity based on field measurements in Amazonian forests (Barlow et al., 2003; Brando et al., 2012; Brando et al., 2014). For needleleaf trees in boreal regions, the fire-induced tree mortality was parameterized by region-specific nonlinear functions of FRP based on satellite observed sensitivity relationships (Rogers et al., 2015).

We illustrate the nonlinear sensitivity relationships between fire-induced tree mortality and FRP over the two boreal continental regions in Figure 7. Previous studies showed that boreal Eurasian forest fires are less intense than that in North America (Wooster & Zhang, 2004) and different fire dynamics and plant traits have significant impacts on tree survival in those regions (Rogers et al., 2015). These regional characteristics of fire intensity and burn severity are evident in satellite measurements (Heward et al., 2013). Therefore, we used satellite-observed FRP and tree mortality data in postfire boreal forest regions and fitted a nonlinear function for each biome based on the medians of statistically resampled data (Figure 7). By implementing region-specific sensitivity relationships, the RESFire model could capture these regional differences and effects of fire disturbances on ecosystem structure and vegetation population. Considering that actual tree mortality is not an instantaneous process, we added fire-induced annual tree mortality fractions into a mortality potential (MP) pool (%) and then withdrew a portion of it at a specific tree MR (*fmr*, %/s) for every modeling time step (equation (29)),

$$\frac{dMP}{dt} = \frac{\sum_{i=1}^{3} MR^i \times BA_{clm}^f \times f^i}{\Delta t} - fmr = \frac{\sum_{i=1}^{3} MR^i \times BA_{clm}^f \times f^i}{\Delta t} - \frac{MP}{tsc}, \tag{29}$$

where Δt is seconds per time step and *fmr* is the instantaneous postfire vegetation MR estimated by the contemporary MP over a time constant (*tsc*) of total seconds per year.

The whole-plant MP pool would almost run out during the following 2 to 3 years if there is no fire and no new MP being added (equation (29)). For those fractional tree/shrub patches that were killed by fires, we deducted the mortality fraction per grid cell from the original PFT fraction value and added the same deducted fraction to grasslands if it exists in the same grid cell, or bare land if no grassland exists in the grid cell. In this way, we can simulate simplified land cover change due to fire-induced vegetation change in the RESFire model. Such variable PFTs with updated ecosystem structures and optical properties would influence surface albedo in the land model and other PFT-related functionality and further trigger a series of radiation, biogeochemical, and hydrological feedbacks after fire occurrence.
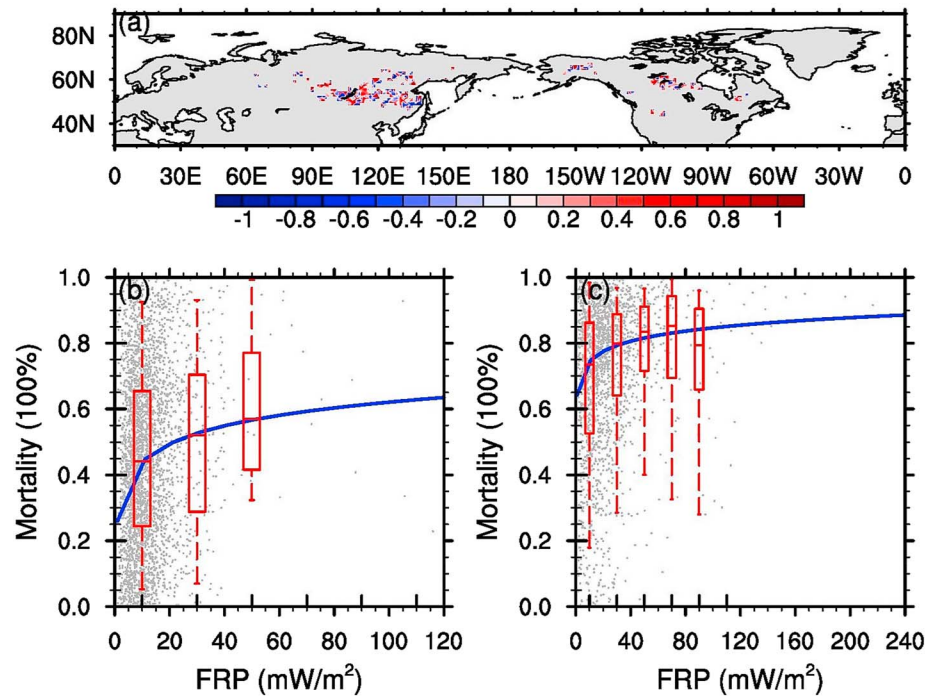
Figure 7. Relationships between fire radiative power (FRP) and boreal tree mortality. (a) The spatial distribution of correlation coefficients between satellite observed FRP and tree mortality; (b) raw gridded data (gray dots), statistical samples (red boxes), and fitted sensitivity relationship (blue line) of FRP and tree mortality over boreal Eurasia; (c) same as (b) but over boreal North America.

Besides mortality, we also considered postfire recovery processes over burned regions. Previous studies suggested that the postfire recovery is mostly a self-replacement process in many burned regions (Epting & Verbyla, 2005; Jin et al., 2012). We only considered stand-replacing processes without interspecies competition during secondary succession and postfire recovery in our model. We collected and averaged the PFT-specific annual fractional recovery rates (RR, %) in Table 6 from several in situ and satellite-based observations for secondary succession. Epting and Verbyla (2005) found that severe burning speeds up vegetation recovery due to reduced competitive pressure in the postfire environment. To incorporate such a positive feedback mechanism, we adjusted the instantaneous PFT recovery rate (frr, %/s) according to the contemporary tree mortality fraction (MF, %) as a surrogate of burning severity (equation (30)),

$$frr = 10 \times MF \times \frac{RR}{tsc} \qquad (30)$$

We applied these adjusted PFT-specific recovery rates in combination with the estimated MR to allow burned ecosystem to recover. Since we did not consider complete vegetation dynamics here, the gridded PFT fractions could only decrease by fire-induced vegetation mortality and then restore back to default prefire levels after full recovery if there is no more fire disturbance. The instantaneous changing rate in PFT fractions (Δf, %/s) at the grid cell level is the difference between fire-induced whole-plant MRs and postfire recovery rates (equation (31)),

$$\Delta f = -\frac{dMF}{dt} = frr - fmr. \qquad (31)$$

2.6. Weather/Climate Model Output Distribution Mapping

The fire modeling performance depends strongly on the quality of fire weather variables. When CAM5 was used to drive the fire model in a
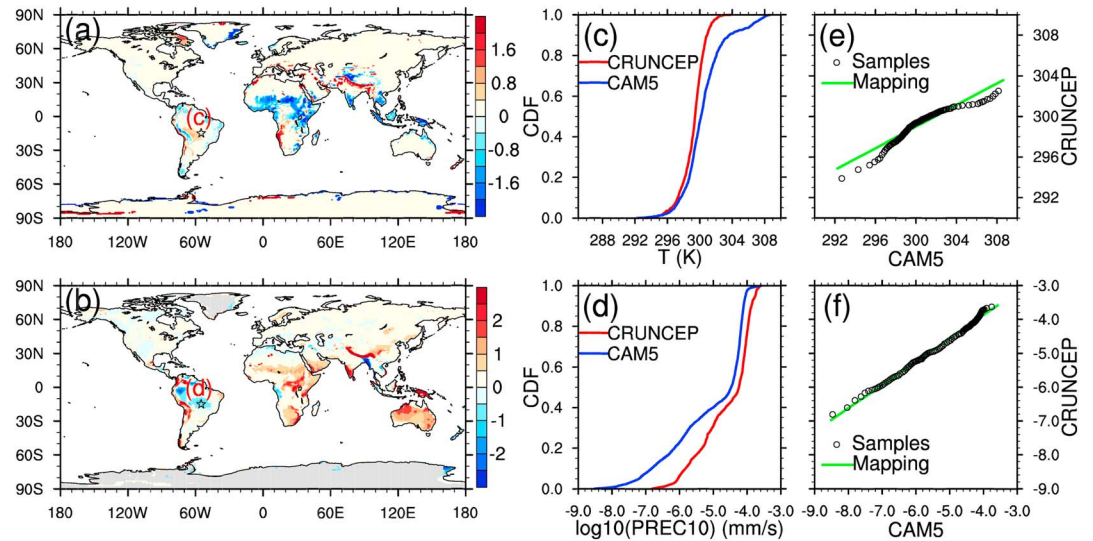
Table 6
Postfire Annualized Recovery Rates for Each PFT Group

PFT	Recovery rates
Shrub	10%[a]
Broadleaf tree (tropical regions)	5%[b,c,d]
Broadleaf tree (boreal regions)	8%[e,f]
Needleleaf tree	15%[f,g,h]

Note. PFT = plant functional type.
[a]Rydgren et al. (2004). [b]Chazdon (2003). [c]Finegan (1996). [d]Guariguata and Ostertag (2001). [e]Beck and Goetz (2011). [f]Epting and Verbyla (2005). [g]Goetz et al. (2006). [h]Jin et al. (2012).

Figure 8. Online fire weather biases and corrections using the distribution mapping method. (a) Spatial distributions of online biases in surface temperature (unit: K); only biases at the 0.05 significance level are shown. (b) Same as (a) but for 10-day running mean precipitation biases (unit: 10^{-5} mm/s). (c) Cumulative distribution function (CDF) of daily surface temperature in a sample grid cell from Climatic Research Unit and National Centers for Environmental Prediction (CRUNCEP) and Community Atmosphere Model version 5 (CAM5); (d) same as (c) but for 10-day running mean precipitation in the same sample grid cell. (e) Samples of daily surface temperature in the sample grid cell from CRUNCEP and CAM5 (circles) and the corresponding mapping function (green line); (f) same as (e) but for logarithmic 10-day running mean precipitation. PREC10 = precipitation.

two-way coupled simulation mode, biased meteorological variables led to significant biases in burned area estimates (to be shown in section 3.1) since all our fire model parameterizations were developed based on the observation-reanalysis atmospheric data. These model biases, especially precipitation-related hydrological biases, are common in the current generation of climate models (Ma et al., 2013; Wang et al., 2014). To reduce negative impacts from atmospheric model biases, we introduced bias corrections in the two-way coupled mode on the basis of a statistical distribution mapping method (Piani et al., 2010; Teutschbein & Seibert, 2012). In general, we first evaluated the online CAM5 modeling performance of gridded fire weather variables (Tables 3 and 6) against the offline counterparts based on the CRUNCEP data of the training period (2003–2006). For grids cells with significant modeling biases, we then obtained the cumulative distribution function of offline daily values based on the observation-reanalysis combined data and online daily values from the CAM5 model. We fitted linear mapping functions based on the two sets of distribution in each grid cell. Lastly, we used the mapping function to project the CAM5 fire weather simulation onto the corresponding values at the same quantile in the reanalysis data (Figure 8). In this way, we reduced climatological mean biases of the CAM5 model simulations while keeping dynamic variability simulated by the model. We transformed precipitation data in a logarithm scale before fitting mapping functions since precipitation intensity spectra usually follow the exponential distribution (Piani et al., 2010).

Figure 8 demonstrates examples of online bias corrections for simulated surface temperature and precipitation, in which we find significantly cool and wet biases over most African regions as well as biased drought conditions over South American rain forest and savanna regions in CAM5 results (Figures 8a and 8b). The cumulative distribution functions in Figures 8c and 8d show such bias tendencies across all quantiles of CAM5 simulated surface temperature and 10-day running mean precipitation in a selected grid cell of South America. We then used mapping functions (Figures 8e and 8f) estimated by linear regressions based on statistical distributions of model and reanalysis data (Piani et al., 2010; Teutschbein & Seibert, 2012) to project the CAM5 simulations onto the reanalysis data at the same percentiles such that the online model weather biases were reduced. In the next section, we designed multiple model simulation experiments and further evaluated the effectiveness of weather bias corrections on fire simulation by comparing both default and bias-corrected fire model results with benchmarks.

Table 7
Modeling Settings of Fire Simulation Experiments

Name	RESFire_CRUNCEPa	RESFire_CRUNCEPb	RESFire_CAM5a	RESFire_CAM5b
Atmosphere forcing	1991–2010 CRUNCEP	1991–2010 CRUNCEP	CAM5 with bias correction	CAM5 without bias correction
Population density	Variable from 1991 to 2010	Fixed in 2000	Fixed in 2000	Fixed in 2000
Lightning	Climatology	Climatology	Climatology	Climatology
Land cover	Semistatic with fire perturbation	Semistatic with fire perturbation	Semistatic with fire perturbation	Semistatic with fire perturbation
Nitrogen and aerosol deposition	Fixed in 2000	Fixed in 2000	Fixed in 2000	Fixed in 2000
Anthropogenic/biogenic emissions	None	None	Fixed in 2000	Fixed in 2000
GHGs	Constant	Constant	Constant	Constant
SST/Sea ice	None	None	Present-day climatology	Present-day climatology

Note. RESFire = REgion-Specific ecosystem feedback Fire; CRUNCEP = Climatic Research Unit and National Centers for Environmental Prediction; CAM5 = Community Atmosphere Model version 5; SST = sea surface temperature.

2.7. Model Simulation Sets and Evaluation Metrics

After model development and implementation, we conducted four sets of fire simulation experiments using RESFire with both CRUNCEP data and CAM5-simulated atmosphere forcing (Table 7). The first two sets were stand-alone land model simulation driven by the 1991–2010 CRUNCEP observation-reanalysis combined atmospheric data, which included global 6-hourly surface temperature, wind speed, specific humidity, air pressure, precipitation, and surface downward solar radiation (Viovy, 2013). We ran these two sets from the same initial spin-up condition to a steady state after several hundred years of land model simulation. The other model input files such as the prescribed climatological cloud-to-ground lightning data, nitrogen and aerosol deposition, and land cover data were also the same except the population density data. We used variable population density from 1991 to 2010 in the first simulation set (RESFire_CRUNCEPa), and we fixed population density at the 2,000-year level in the second simulation set (RESFire_CRUNCEPb). Therefore, the interannual variability of fire simulation in RESFire_CRUNCEPa was driven by both natural and anthropogenic forcing, while it was driven by only natural forcing in RESFire_CRUNCEPb. By comparing the difference between these two sets, we isolated the anthropogenic constraint effects simulated in the fire model. The last two sets were two-way coupled simulations with online CAM5 atmosphere model and CLM4.5 land model. The first coupled simulation set (RESFire_CAM5a) was run for 10 years driven by bias corrected fire weather from the CAM5 atmosphere simulation. The second coupled simulation set (RESFire_CAM5b) did not include bias corrections. By comparing these two experiments, we evaluated the effects of the online bias correction method. We ran both online coupled experiments for 10 years from the same initial conditions of the stand-alone experiments. All other model input data including population density, GHG concentrations, and nitrogen and aerosol deposition rates were the same with RESFire_CRUNCEPb. The cyclical 3-hourly lightning data were interpolated from the NASA LIS/OTD grid product v2.2 2-hourly climatological lightning data with the cloud-to-ground lightning fractions calculated based on Prentice and Mackerras (1977). The population density data were derived from the Gridded Population of the World version 3 (CIESIN & CIAT, 2005). The land use and land cover change data were

Table 8
Fire Modeling Benchmark Metrics and References

Category	Variable	Data set	Spatial/temporal resolution
Intensity	Burned area	GFED4.1s[a,b] (1997–2010)	0.25° × 0.25°; monthly
	Emissions	GFED4.1s[a,b,c] (1997–2010)	0.25° × 0.25°; monthly
	FRP	MODIS active fire products[d] (2003–2010)	0.5° × 0.5° derived from MODIS products at native 1-km resolution; monthly
Impacts	Plant mortality	MODIS remote sensing products[e] (2001–2009)	0.25° × 0.25° derived from MODIS products at native 250, 500, or 1 km resolution; annual
	Ecosystem resilience	In situ data[f] (1850–2004)	Canadian boreal forest sites; decadal

Note. GFED = Global Fire Emissions Database; FRP = fire radiative power; MODIS = Moderate Resolution Imaging Spectroradiometer.
[a]Giglio et al. (2013). [b]Randerson et al. (2012). [c]van der Werf et al. (2017). [d]Giglio et al. (2006). [e]Rogers et al. (2015). [f]Goulden et al. (2011).
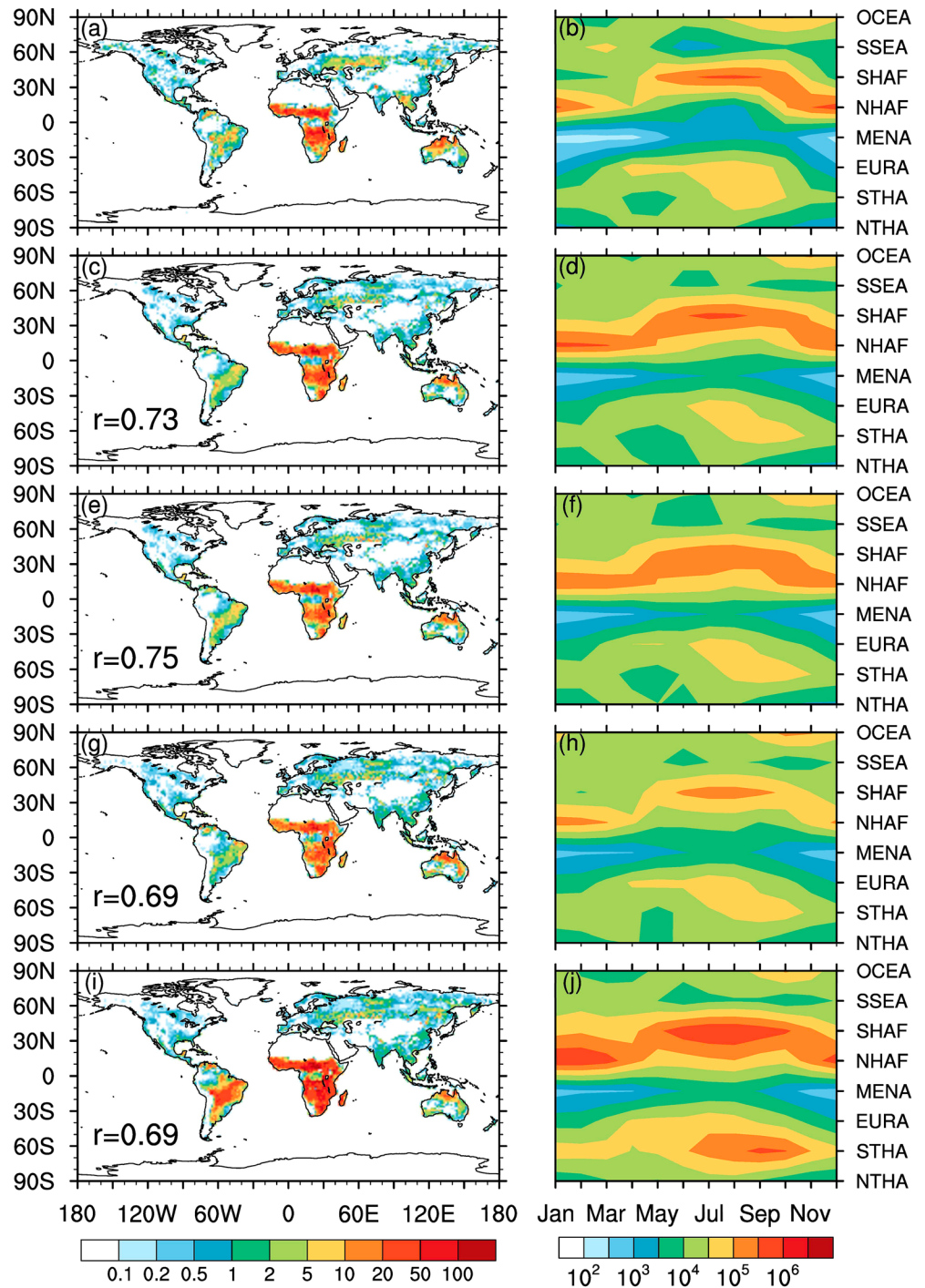
Figure 9. Comparisons of spatial distributions and seasonal variations of burned area in the observations and simulations. (a) GFED4.1s burned area fractions (%) averaged from 1997 to 2010; (b) seasonal variations of averaged GFED4.1s burned areas (km²) in the eight subregions; (c, d) same as (a, b) but from RESFire_CRUNCEPa; (e, f) same as (a, b) but from RESFire_CRUNCEPb; (g, h) same as (a, b) but from RESFire_CAM5a; (i, j) same as (a, b) but from RESFire_CAM5b. The spatial correlation coefficients between simulated global burned area fractions and the GFED4.1s data are shown on the bottom left corners of (c), (e), (g), and (i). RESFire = REgion-Specific ecosystem feedback Fire; GFED = Global Fire Emissions Database; CRUNCEP = Climatic Research Unit and National Centers for Environmental Prediction; CAM5 = Community Atmosphere Model version 5.
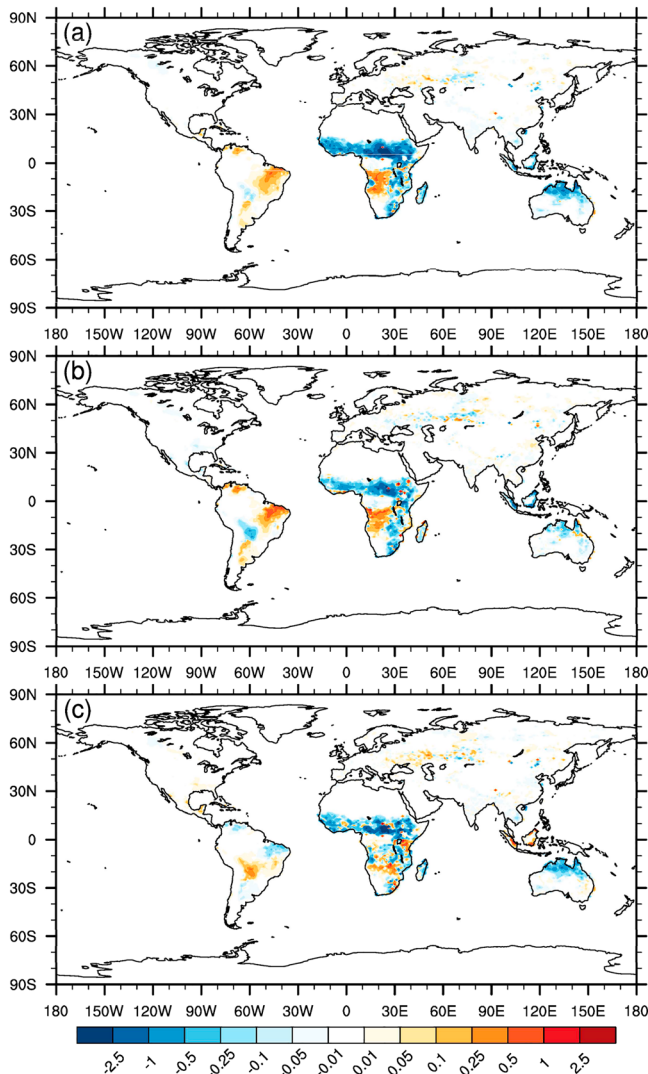
Figure 10. Comparisons of decadal trends (%/year) in annual averaged burned areas from 1991 to 2010. (a) Burned area trends driven by natural and demographic forcing in RESFire_CRUNCEPa with changing weather and population; (b) burned area trends driven by only natural forcing in RESFire_CRUNCEPb with changing weather but fixed population; (c) burned area trends driven by demographic changes. RESFire = REgion-Specific ecosystem feedback Fire; CRUNCEP = Climatic Research Unit and National Centers for Environmental Prediction.

based on the 2,000-year data from version 1 of the Land-Use History A product (Hurtt et al., 2006). The semistatic PFT types did not change for each model grid cell except fire induced PFT (area) fraction variations due to tree mortality and recovery in RESFire. The monthly nitrogen and aerosol deposition data were taken from CESMv1.2 full chemistry simulation results (Hurrell et al., 2013). We also used the anthropogenic and biogenic emissions in 2000 (Lamarque et al., 2010) and prescribed present-day climatological sea surface temperature and sea ice data (Hurrell et al., 2008) in the last two coupled experiments. All these model inputs at different spatial and temporal resolutions were interpolated to the modeling grids at the half-hourly time step to drive the CLM land model simulation. The stand-alone model settings, especially the RESFire_CRUNCEPa experiment, are similar with previous CLM4.5-fire simulation studies (Li et al., 2012, 2013, 2014).

We used the International Land Model Benchmarking (ILAMB) system (Luo et al., 2012) to evaluate the RESFire modeling results of fire behavior and impacts. The ILAMB system is an integrated land model benchmarking system designed to improve the performance of land models and to reduce key uncertainties in land surface processes. As one of the major uncertainty sources in land models, fire simulation has considerable influences on the modeling of biogeochemical, biophysical, and hydrological processes. We evaluated the RESFire results in the context of burned area, fire emissions, and ecosystem effects to provide a comprehensive evaluation of fire model performance. Table 8 lists the benchmark metrics and their sources used for model evaluation.

3. RESFire Model Evaluation

3.1. Burned Area

We examined both spatial distributions and seasonal variations of global and regional burned areas in stand-alone and two-way coupled modes in Figure 9. The spatial correlation coefficients range from 0.69 to 0.75 on a global basis in different fire simulation experiments, which are comparable with the LL2013 fire model performance ($r = 0.71$; Li et al., 2014). We also compared the model simulations on a regional basis and listed the regional spatial correlations between each experiment and GFED4s data in Table S4. The stand-alone modeling results driven by the CRUNCEP atmosphere data (Figures 9c and 9e, RESFire_CRUNCEPa/b) outperform the two-way coupled modeling results driven by CAM5 meteorological inputs (Figure 9g, RESFire_CAM5a with bias corrections; Figure 9i, RESFire_CAM5b without bias corrections). After bias corrections in fire weather, the RESFire_CAM5a results show considerable burned area bias reductions in all seasons over most regions, especially Africa and South America, comparing to the RESFire_CAM5b results. For instance, the high bias in surface temperature and low bias in precipitation over the central South America region result in an unrealistic drought environment in the default CAM5 simulation, which leads to a high bias in burned area estimates. The bias correction module in RESFire reduces biases in CAM5 fire weather data and improves the fire modeling performance with reduced deviation from the benchmark over this region. The seasonal variation estimates are also significantly better in stand-alone RESFire_CRUNCEPa/b (Figures 9d and 9f) and online bias-corrected RESFire_CAM5a results (Figure 9h) than default RESFire_CAM5b results (Figure 9j). Figure S3 shows comparisons of time series of annual burned areas for each region in RESFire_CRUNCEPa and GFED4.1 s. The model results agree quite well with the GFED data on a global basis, though discrepancies are significant in some regions like boreal north America, central Asia, and southeast Asia. Those biases might result from insufficient natural and

Table 9
ILAMB Evaluation Results for Burned Area Estimates Using GFED4s as the Benchmark

Metrics	Units	GFED4s	CLM45bgc _CRUNCEP	RESFire _CRUNCEPa	RESFire _CRUNCEPb	RESFire _CAM5a	RESFire _CAM5b
Annual mean	Mha/year	485.49	315.66	464.72	478.88	471.77	1033.62
Bias	Mha/year	—	−169.84	−20.77	−6.61	−13.72	548.13
Relative bias	100%	—	−0.35	−0.04	−0.01	−0.03	1.13
RMSE	Mha/month	—	87.19	80.33	79.06	82.95	126.52
Phase	months	—	1.35	0.50	0.51	0.55	0.58
Global bias score	—	—	0.50	0.59	0.59	0.57	0.53
RMSE score	—	—	0.42	0.45	0.45	0.45	0.39
Phase score	—	—	0.75	0.82	0.82	0.82	0.82
Taylor score	—	—	0.36	0.85	0.82	0.78	0.56
Interannual score	—	—	0.55	0.56	0.56	0.55	0.52
Overall score	—	—	0.50	0.62	0.61	0.60	0.53

Note. ILAMB = International Land Model Benchmarking; GFED = Global Fire Emissions Database; RESFire = REgion-Specific ecosystem feedback Fire; CRUNCEP = Climatic Research Unit and National Centers for Environmental Prediction; CAM5 = Community Atmosphere Model version 5; RMSE = root mean square error.
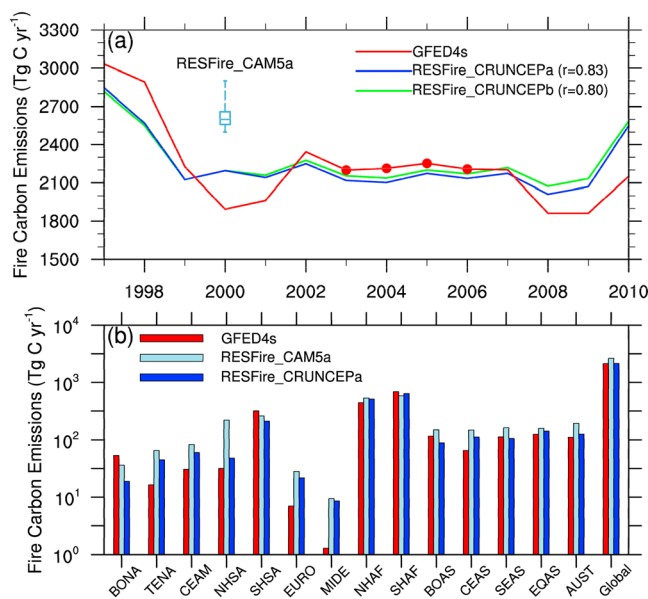

Figure 11. Comparisons of interannual fire carbon emissions. (a) Temporal variations of annual fire carbon emissions from GFED4.1s and RESFire_CRUNCEPa/b with the temporal correlation coefficients shown in the parenthesis. The red dots denote the years of observations used for fire model training. Statistical results from RESFire_CAM5a under the 2000-year climate conditions are shown in the box for comparison. (b) Regional and global annual fire carbon emissions from GFED4.1s, RESFire_CRUNCEPa, and RESFire_CAM5a. The 14 regions are the same with the GFED data set (Giglio et al., 2010). BONA = Boreal North America; TENA = Temperate North America; CEAM = Central America; NHSA = Northern Hemisphere South America; SHSA = Southern Hemisphere South America; EURO = Europe; MIDE = Middle East; NHAF = Northern Hemisphere Africa; SHAF = Southern Hemisphere Africa; BOAS = Boreal Asia; CEAS = Central Asia; SEAS = Southeast Asia; EQAS = Equatorial Asia; AUST = Australia and New Zealand; RESFire = REgion-Specific ecosystem feedback Fire; GFED = Global Fire Emissions Database; CRUNCEP = Climatic Research Unit and National Centers for Environmental Prediction; CAM5 = Community Atmosphere Model version 5.

anthropogenic triggers for specific fire types including large wildfires, agricultural fires, and deforestation fires in these regions, which are a limitation of the current model.

To illustrate the natural forcing and socioeconomic effects in RESFire, we examined the decadal trends in global burned areas from RESFire_CRUNCEPa and RESFire_CRUNCEPb and compared their differences in Figure 10. It is noted that RESFire_CRUNCEPa includes both interannually changing natural and anthropogenic impacts, while RESFire_CRUNCEPb with fixed population density only includes the varying fire weather influence. Figures 10a and 10b show similar patterns of burned area trends during the 1991–2010 period, which implies natural forcing as a dominant factor for decadal changes over most regions. We found opposite trends between the Northern and Southern Hemispheric Africa with decreasing and increasing burned areas over the past two decades, respectively. Such contrasting changes are consistent with previous findings based on satellite observations. Andela and van der Werf (2014) found similar downward and upward trends over Northern and Southern Hemispheric Africa and attributed these changes to the shifted precipitation patterns due to the phase change of the El Niño/Southern Oscillation. They also concluded that the climate impact of precipitation changes contributed most (51%) to the upward trend over Southern Hemispheric Africa, while the impact of demographic and socioeconomic changes (20%) were almost as important as the precipitation changes (24%) over Northern Hemispheric Africa. Our modeling results corroborate these findings in the comparison of RESFire_CRUNCEPa and RESFire_CRUNCEPb results. Figure 10c shows the difference of RESFire_CRUNCEPa from RESFire_CRUNCEPb, which indicates the demographic effect. In Northern Hemispheric Africa, the negative trend in Figure 10c is almost comparable to the negative trend driven by only natural forcing in Figure 10b, suggesting nearly equivalent contributions from demographic (Figure 10c) and climate change (Figure 10b) factors to the total trend in Figure 10a. In contrast, the much weaker positive changes over Southern Hemispheric Africa in Figure 10c imply that the regional increasing trend in Figure 10a is dominated by natural forcing as shown in Figure 10b. In contrast, the fire trends by natural and

Table 10
Comparisons of Annual Averaged Fire Emissions with Standard Deviations of Interannual Variability

Species (Tg/year)	GFED4s	RESFire_CRUNCEPa	RESFire_CAM5a
Carbon	2235 ± 346	2199 ± 186	2629 ± 106
CO_2	7574 ± 1133	7518 ± 817	8421 ± 426
CO	365 ± 81	408 ± 61	446 ± 23
CH_4	16 ± 6	21 ± 5	21 ± 1.2
NMHC	18 ± 2	25 ± 2	27 ± 1.2
H_2	10 ± 1.9	11 ± 1.5	12 ± 0.6
NO_x	15 ± 1.8	14 ± 1.2	16 ± 0.8
N_2O	0.95 ± 0.15	0.78 ± 0.09	0.87 ± 0.04
$PM_{2.5}$	37 ± 6	37 ± 4	40 ± 2
TPM	48 ± 8	54 ± 6	59 ± 3
TC	19 ± 3.7	19 ± 2.4	21 ± 0.9
OC	17 ± 3	17 ± 2	19 ± 0.9
BC	1.9 ± 0.3	2.5 ± 0.2	2.7 ± 0.1

Note. GFED = Global Fire Emissions Database; RESFire = REgion-Specific ecosystem feedback Fire; CRUNCEP = Climatic Research Unit and National Centers for Environmental Prediction; CAM5 = Community Atmosphere Model version 5.

demographic forcings in South America and Southeast Asia have opposite signs in most regions, and the former is more dominant. Over northern Australia, on the other hand, fire suppression by the demographic factor is most important (~75%). In general, population increases tend to suppress fires at the global scale, while natural forcing can either enhance or suppress fires at regional scales, which agree with observation-based findings (Andela et al., 2017; Andela & van der Werf, 2014).

To provide a more quantitative understanding of modeling performance, we applied the ILAMB system to evaluate the RESFire results with different experiment settings and quantified burned area modeling scores using multiple metrics, which include absolute and relative biases, seasonal phase, interannual variability, RMSE, and Taylor score in Table 9 (see the supporting information for details of evaluation metrics); the GFED4s data set (2001–2010) was used as the benchmark. For comparison, we also listed the evaluation results of the default CLM LL2013 fire scheme driven by the same data atmosphere forcing named as CLM45bgc_CRUNCEP. It is noted that the default CLM LL2013 fire model was calibrated using different atmospheric reanalysis data (Qian et al., 2006) and an old version of the GFED data set (GFED3) as benchmarks (Giglio et al., 2010; van der Werf et al., 2010), and the simulation period was different from this work (1997–2004 in Li et al., 2014, vs. 1991–2010 here). Though Li and Lawrence (2017) recalibrated the LL2013 fire model in CLM recently, the updated CLM-fire model released with the new version of CESM was not available during the model development period of this paper. Therefore, our CLM45bgc_CRUNCEP run is based on the same version of LL2013 without recalibration and its burned area result (316 Mha/year) is very close to the published one (322 Mha/year) in Li et al. (2014). This similarity suggests the correspondence of our CLM45bgc_CRUNCEP simulations with the previous published ones (Li et al., 2013, 2014). As shown in the table, the burned area simulations in the RESFire model in both stand-alone and two-way coupled modes outperform the default fire scheme in most benchmarking metrics, such as absolute and relative annual mean biases and phase variations. The smaller spatial and temporal biases and higher scores in the RESFire results corroborate the previous comparisons in Figure 9. By comparing the evaluation results between online modeling results with (RESFire_CAM5a) and without bias corrections (RESFire_CAM5b), we also found significant improvements in all benchmarking metrics after implementing fire weather bias corrections. In general, the overall modeling score as a weighted average of all metrics (see supporting information for details) increases from 0.50 of CLM45bgc_CRUNCEP to 0.62/0.61 of RESFire_CRUNCEPa/b and 0.60/0.53 of RESFire_CAM5a/b, respectively. Such increases in modeling scores are robust if we change the evaluation benchmark to the old GFED3 data set used for the LL2013 fire model development and calibration (see Table S3). These results illustrate the improved modeling capability of the RESFire model driven by either offline reanalysis or online simulation data, which is crucial for both fire hindcast or future projection studies. Considering sensitivity experiment objectives and model setting limitations of RESFire_CRUNCEPb and RESFire_CAM5b, we mainly focused on the evaluation and comparison of the more comprehensive RESFire_CRUNCEPa (with fully natural and anthropogenic forcing) and RESFire_CAM5a (with bias correction) data in the following sections to demonstrate the RESFire modeling capability.

3.2. Fire Emissions

We evaluated the interannual variability of fire carbon emissions and compared annual mean carbon emissions with the GFED4.1 s data for each subregion (Figure 11). Similar to the burned area estimates, the simulated fire carbon emissions also agree well with the benchmark data with temporal correlation coefficients of 0.80~0.83 in the RESFire_CRUNCEPa/b results driven by the reanalysis-observation-based atmosphere forcing. The fire model captures the two high fire years around 2000 and 2008 as shown in the GFED data, and RESFire_CRUNCEPa (-24 Tg C/year^2) with variable natural and anthropogenic forcing better reproduces the downward trend in global averaged GFED fire emissions (-50 Tg C/year^2) than RESFire_CRUNCEPb (-18 Tg C/yr^2) with fixed population and demographic effects. These differences are consistent with the
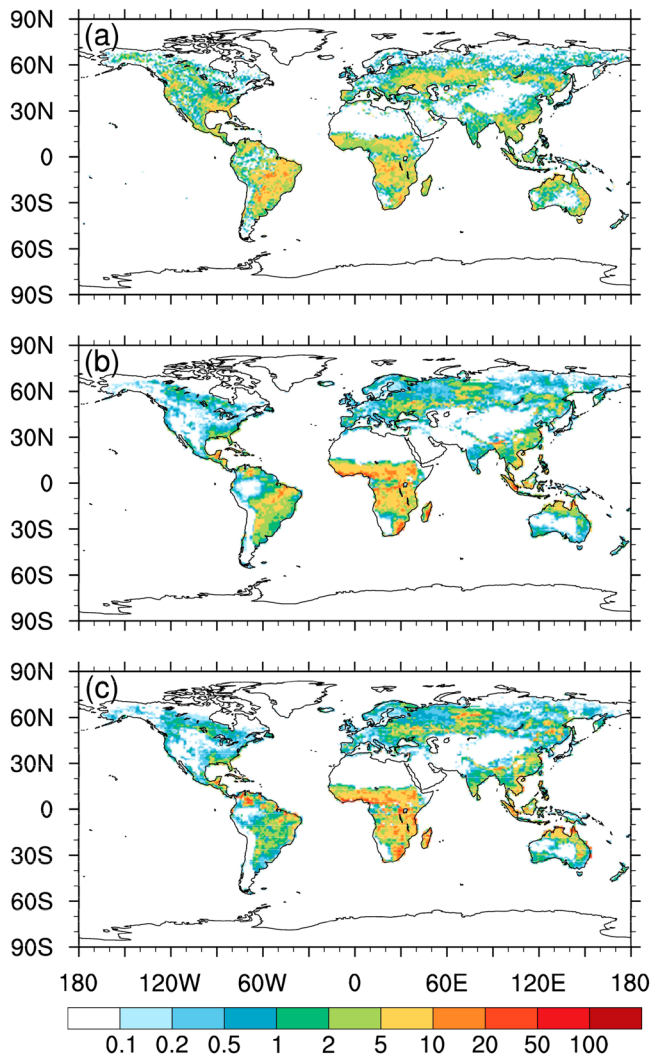
Figure 12. Comparisons of observed and simulated FRP averaged from 2003 to 2010. (a) Annual average FRP (mW/m²) based on Aqua MODIS observations; (b) and (c) are the same as (a) but based on RESFire_CRUNCEPa and RESFire_CAM5a, respectively. RESFire = REgion-Specific ecosystem feedback Fire; CRUNCEP = Climatic Research Unit and National Centers for Environmental Prediction; FRP = fire radiative power; MODIS = Moderate Resolution Imaging Spectroradiometer.

trend comparison results in Figure 10. It is worth noting that we only trained the RESFire model with the 4-year data from 2003 to 2006, which show less interannual variation than the other years. The successful reconstruction of large variations in the other years demonstrated the effectiveness of RESFire. Since the simulated atmosphere internal variability in CAM5 does not necessarily represent the interannual variability of real atmosphere, we only examined the statistical properties of RESFire two-way coupled results with bias corrections (RESFire_CAM5a). The 10-year-averaged RESFire_CAM5a carbon emissions are larger than the GFED4.1 s and RESFire_CRUNCEPa by 18% and 20%, respectively. High bias regions include temperate North America, Northern Hemispheric South America, Europe, and Middle East (Figure 11b). One consequence is that the tendency of underestimating fire-induced aerosol loading (Ward et al., 2012) was not severe in the online CAM5 simulation. The published LL2013 CLM4.5-fire carbon emission is 2.1 Pg C/year averaged from 1997 to 2004 (Li et al., 2014), which is lower than our results here, but we should point out again that such biases could result from different atmosphere forcing data and modeling benchmarks used in LL2013.

In Table 10, we examined the averaged fire emissions (1997–2010) of specific trace gases and aerosol species. The default CLM45bgc_CRUNCEP does not provide fire emissions for each species, so we only compared complete forcing-driven RESFire_CRUNCEPa and online bias-corrected RESFire_CAM5a results with the GFED4.1s data. Both modeling outputs show good agreement with the benchmark data in most species. It is also noted that RESFire_CAM5a results have lower interannual variability than observations in GFED, which can be attributed to the fixed climate forcing such as prescribed sea surface temperature, sea ice conditions, and anthropogenic/biogenic emissions in the online coupled experiment.

We then compared spatial distributions of simulated FRP distributions against satellite observations (MYD14CMH) onboard Aqua MODIS (Giglio et al., 2006) in Figure 12. All data are annual averages from 2003 to 2010. The uncertainties in the conversion factors also contribute to the discrepancies between the observations and simulation results. Both stand-alone RESFire_CRUNCEPa and two-way couple RESFire_CAM5a results have low biases in most regions except over Africa, where the simulation results are overestimated to some extent. However, the uncertainty in the fire FRP estimation is smaller than that in the sensitivity relationships between observed FRP and tree mortality (see Figure 7 for example), which implies that the uncertainty from the latter source would dominate the total uncertainty in tree mortality simulation. Therefore, we suggest focusing on the FRP-mortality sensitivity parameterization to further improve the model in the future. We examined the fire-related tree mortality and regrowth in the next section to demonstrate the RESFire capability of modeling fire feedbacks to ecosystems.

3.3. Ecosystem Responses

Since the tree mortality-induced albedo changes are most significant at high-latitude regions with snow cover (Jin et al., 2012; Randerson et al., 2006), we mainly compared the simulated tree mortality with the satellite data over boreal regions. These regions also show considerable continental differences between North America and Eurasia in fire dynamics as well as ecosystem and climate feedbacks (Rogers et al., 2015). Similar to the satellite observations, the RESFire mortality results show higher MRs in North America and lower MRs over Eurasia (Figure 13). Such differences result from different fire behavior and plant traits. To be specific, North American fires are characterized by more crown fires with higher
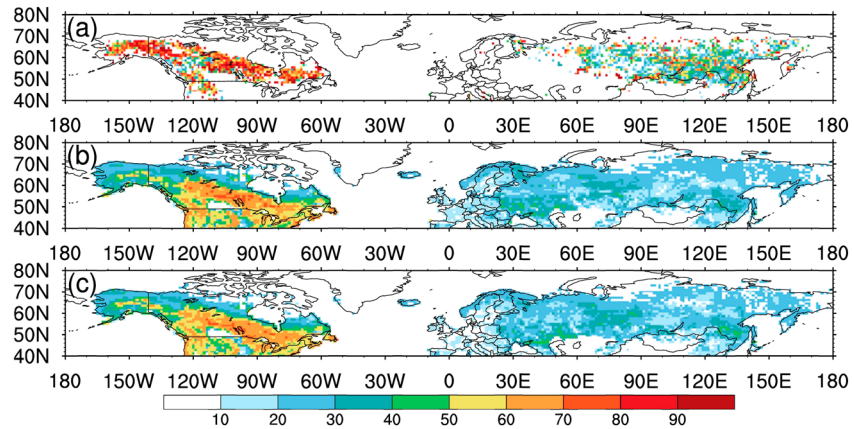
Figure 13. Comparisons of fire induced fractional tree mortality rates (%) in satellite observations and model simulations. (a) Annual averaged tree mortality rates based on satellite observations from 2001 to 2009; (b) annual averaged tree mortality rates in fire seasons over the same period based on RESFire_CRUNCEPa; (c) same as (b) but based on the 10-year averaging results of RESFire_CAM5a under the 2000 climate conditions.
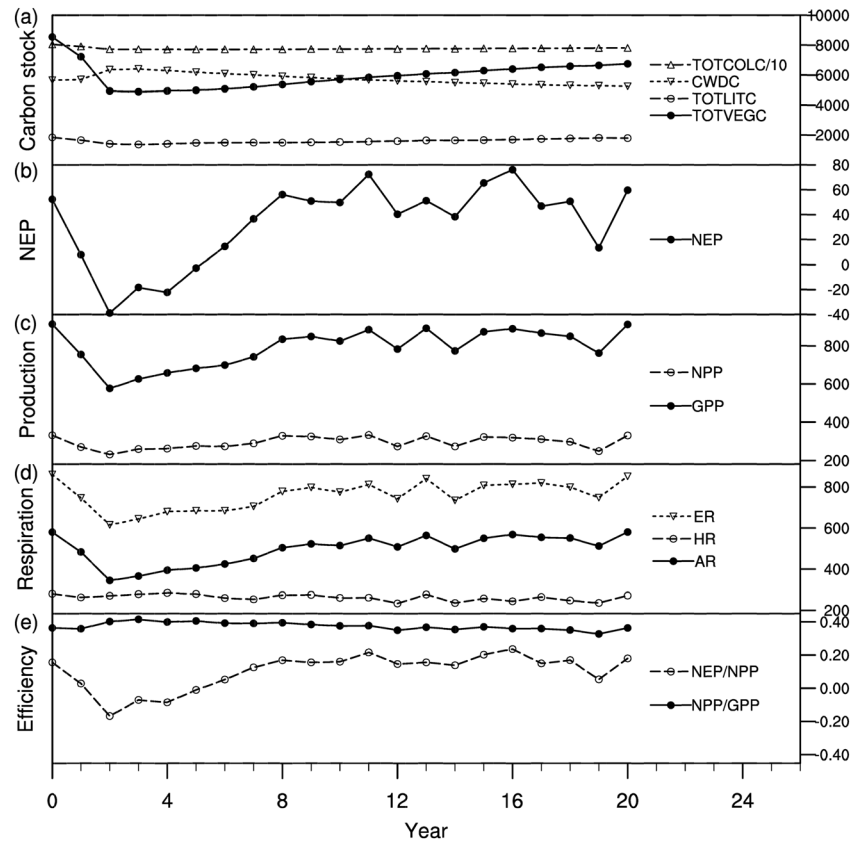

Figure 14. Simulated postfire temporal evolution of carbon budget and ecosystem productivity based on the idealized burning experiment. (a) Total column carbon (g C/m^2), coarse woody debris carbon (g C/m^2), total litter carbon (g C/m^2), and total vegetation carbon (g C/m^2); (b) net ecosystem production (g C·m^{-2}·year^{-1}); (c) net primary production (g C·m^{-2}·year^{-1}) and gross primary production (g C·m^{-2}·year^{-1}); (d) total ecosystem respiration (g C·m^{-2}·year^{-1}), heterotrophic respiration (g C·m^{-2}·year^{-1}), and autotrophic respiration (g C·m^{-2}·year^{-1}); (e) ecosystem carbon storage efficiency (unitless) and plant production efficiency (unitless). The time of fire disturbance is at year 0.

Table 11
Comparisons Between the RESFire and LL2013 Fire Models

Fire model		The LL2013 fire model[a]	RESFire
Occurrence	Ignition	Climatological lightning and anthropogenic triggers	Climatological lightning and anthropogenic triggers
	Flammability	A global function of fuel load, RH, and soil wetness	Region- and PFT-specific functions of fuel load, T10, PREC10, and soil water
	Suppression	Functions of population density and GDP	Region- and PFT-specific functions of population density and a global unified function of GDP
Spread	Spread rate	A function of wind speed and fuel wetness	Functions of wind speed and fuel wetness
	Duration	Fixed (1 day)	Fixed (1 day)
	Combustibility	A function of root zone soil wetness and RH	Region- and PFT-specific functions of T, RH, SW, and FWET
	Suppression	Functions of population and GDP	Region- and PFT-specific functions of population and global unified function of GDP as well as passive constraints from terrain and landscape fragmentation
Impact	Emissions	Carbon emissions at surface	Carbon, trace gas and aerosol emissions with plume rise estimation and land-atmosphere coupling
	Ecosystem disturbance	Partial vegetation mortality with fixed mortality rates for each part (leaf, stem, root, etc.)	Partial vegetation mortality and fire intensity sensitive whole-plant mortality, PFT dependent recovery, and fire induced land cover changes
	Radiation budget	None	Sensible and latent heat fluxes

Note. RESFire = REgion-Specific ecosystem feedback Fire; PFT = plant functional type; PREC10 = precipitation; T10 = surface temperature; RH = relative humidity; GDP = gross domestic production; SW = surface soil wetness; FWET = fraction of wet canopy.
[a]Li et al. (2012, 2013).

intensity and severity, while Eurasian fires are dominated by surface fires with lower intensity and severity (Rogers et al., 2015). The tree species with high resistance to fire burning are also predominant in Eurasia. Both factors lead to the different tree MRs in response to fires. The model therefore captures the contrast of tree MRs between the two regions, though the model underestimates the MRs in Alaska and Siberia due to the low biases in burned area and FRP estimates. Such low biases are due to underestimated natural and anthropogenic fire triggers in the model with low lightning frequency and population density over these regions. While the current implementation of tree mortality will require further improvement, we note that if only partial vegetation mortality was included, the model simulated recovery rates would be too high since the reduction of leaf area index would enhance light use efficiency of photosynthesis. Including the whole-plant mortality provides longer and more realistic regrowth time estimates.

To evaluate temporal variability of postfire ecosystem recovery, we followed previous studies (Kelley et al., 2014) and designed an idealized burning scenario by introducing single-year burning events in fire peak months of each typical fire-prone region. Figure 14 shows the simulated fire disturbance and postfire evolution of carbon stocks and ecosystem productivity in the context of production, respiration, and efficiency in a sample grid cell of Canadian boreal forest region (Manitoba: 261°E, 56°N). We chose this site to compare modeling results with theoretical trends as well as in situ and satellite observations in previous studies (Goulden et al., 2011; Hicke et al., 2003). The dominant boreal tree species of Manitoba are black spruce, jack pine, and trembling aspen, while vegetation varies with stand age and soil drainage (Bond-Lamberty et al., 2002). Goulden et al. (2011) examined the temporal variations of boreal forest production and respiration during secondary succession after stand-replacing crown fires. They compared the stand observations with theoretical trends and concluded the transition of postfire forest stands from carbon source to sink within 11–12 years. Hicke et al. (2003) assessed the impact of fires on NPP in the North American boreal forest using satellite observations and estimated a similar mean NPP recovery period of about 9 years. The model simulation shows that the total vegetation carbon (TOTVEGC, g C/m^2) decreased substantially after fire disturbances because of the implemented plant mortality and fire carbon emission losses. In contrast, the coarse woody debris carbon (CWDC, g C/m^2) was estimated to increase as a result of plant mortality. With more loss of productive vegetation, the simulated photosynthesis capability of the ecosystem decreased considerably, leading to significantly lower gross primary production (GPP, g C·m^{-2}·year^{-1}) and net ecosystem production (NEP, g C·m^{-2}·year^{-1}). However, the net primary

production (NPP, g C·m^{-2}·year^{-1}) changes were less significant than GPP due to reduced ecosystem competition and respiration consumption after the simulated fire incident with large fractions of whole-plant mortality in the model grid cell. Given the estimates of similar reductions in both GPP and autotrophic respiration (AR, g C·m^{-2}·year^{-1}), simulated NPP only had minor changes, which led to enhanced production efficiency in NPP/GPP (unitless). The simulated rates of above changes decreased with time after the fire disturbance and the ecosystem properties were restored to the prefire condition around two decades later except TOTVEGC. This is because the vegetation carbon accumulated slowly and required more years to fully restore to the prefire level. The simulated postfire ecosystem evolution had similar variations in other regions, though the recovery rates are different for other PFT groups (see Figure S4). In general, the mean recovery periods of postfire forest are about 3–18 years with a transition from carbon source to sink in different PFT regions. These simulations in the idealized experiment are consistent with both theoretical trends and observed variations in previous studies (Goulden et al., 2011; Hicke et al., 2003), suggesting good modeling performance in ecosystem responses to fires.

4. Conclusions and Future Directions

We developed a RESFire model that explicitly considers regional differences in fire behavior and impacts. We refined the fire occurrence and spread parameterizations and added online fire weather bias corrections as well as ecosystem effects in the model. The ILAMB benchmarking results of the RESFire simulations show significant improvements of burned area estimates in both the stand-alone mode driven by offline CRUNCEP atmosphere data and two-way coupled mode driven by online CAM5 atmosphere simulations. The overall fire modeling score increases from 0.50 of the default CLM LL2013 fire scheme to 0.61–0.62 of RESFire_CRUNCEP and 0.53–0.60 of RESFire_CAM5 with improved spatial distributions and temporal variations of fire activities. We applied the RESFire model with observation- and reanalysis-based data to understand the global fire trends from 1991 to 2010. In general, population increases tend to suppress fires at the global scale while natural forcing can either enhance or suppress fires at regional scales. The estimated demographic fire suppression effects are most prominent in Northern Hemispheric Africa (~59%) and northern Australia (~75%). The fire impact evaluation results also demonstrate good modeling capability in simulation of fire emissions and energy fluxes. The mean annual fire carbon emissions of RESFire agree well with the latest GFED4.1s data within 18% in both stand-alone and two-way coupled modes. Fire emissions for gaseous and aerosol species as well as heat fluxes show generally good agreement with benchmarking data. With the implementation of whole-plant mortality and ecosystem recovery, the simulation of fire effects on ecosystems and land cover captures multiple long-term post-fire impacts such as increasing surface albedos in boreal forests with decreasing radiative forcing (Randerson et al., 2006; see Figure S5). The simulated spring albedo changes agree better with satellite observations in Eurasia than North America, which is mainly attributed to low biases of burn area and fire severity simulation in boreal forests of North America. We summarized the comparison between the RESFire model in this work and the default CLM LL2013 fire model in Table 11. These advanced modeling features with fully interactive climate-fire-ecosystem feedbacks are essential to understand the role of fires in climate and ecosystem changes.

A fully interactive fire-climate model such as RESFire is ultimately constrained by the formulation of the land surface model (the CLM in CESM). The PFT-based land model structure of the CLM4.5 is a major limiting factor in the RESFire development to represent complex fire dynamics and fire impacts in a global climate model. CLM4.5 prescribes only one single average of each PFT. It is therefore impossible to distinguish different plant traits such as vegetation species, bark thickness, and stem diameters in the same PFT, which are essential to simulate plant survival and regrowth after fires. The current RESFire implementation can be greatly refined when dynamic global vegetation modeling is implemented in the land model of the CESM. We note that the newly released CESM2 model included an optional cohort-based Functionally-Assembled Terrestrial Ecosystem Simulator of vegetation competition and coexistence with its CLM5 land component, which could be used in the future to improve the RESFire model. The fire weather bias correction applied in this study is most appropriate for the current atmosphere. When it is applied to a future projection, an implicit assumption is that the biases in future projections are similar to the present. While it is imperfect, we think that the large biases in fire estimates without making such corrections of the present atmosphere suggest that it is necessary. We note that the fire model does not include such corrections; that is, the fire model is calibrated using the present atmosphere data directly, essentially making the same

assumption when it is applied in climate projections (or historic hindcasts at preindustrial times). An alternative approach is to use simulated atmosphere data to tune the fire model in the online coupled mode in the same manner of using reanalysis and observation-based atmosphere data. However, such tuning method would result in different versions of fire models tied to specific atmosphere forcing data, which increases the model complexity and reduces its universality. Though the current fire weather bias corrections may need "remapping" of atmospheric modeling data if major changes or updates occur in atmosphere models, it does not necessarily require corresponding changes in the fire model itself. We suggest that future fire model development consider the following issues:

(1) Large uncertainties in fuel load and emission factors undermine the accuracy of fire emission products. Figure S6 compares the CLM fuel load simulation to 176 in situ measurements worldwide (van Leeuwen et al., 2014). The comparison results reveal generally well-simulated biomass fuel, although some discrepancies are still significant in regions such as western North America. Reducing fuel load biases and emission factor uncertainties will better complement the improved burned area simulation in the fire model.

(2) More detailed burning process parameterization is needed to simulate different fire combustion stages. It is known that flaming and smoldering are two burning stages that have very different emission characteristics. Treatment of burning states will improve the model simulation of fire gaseous and particulate emissions and their effects on weather and climate.

(3) Fire impact parameterization for fire-induced plant mortality and regrowth can be improved by including multiple plant traits such as tree species, stem size, and bark thickness. The detailed vegetation demographic information under the PFT-based modeling structure would further improve the modeling capability of regional differences in fire disturbance and ecosystem responses. Approaches such as "cohorts," which aggregate plant individuals with similar size, type, and successional status (Fisher et al., 2015), will allow more detailed fire model development.

(4) More fire-related observations for plant mortality and recovery are needed to improve the fire impact simulation by considering variable recovery rates and interspecies competition. We only considered stand-replacing postfire recovery without changing vegetation dynamics in this work. Integration of the fire model with DGVMs will be needed to fully simulate fire-vegetation dynamics in TEMs.

References

Akagi, S. K., Yokelson, R. J., Wiedinmyer, C., Alvarado, M. J., Reid, J. S., Karl, T., et al. (2011). Emission factors for open and domestic biomass burning for use in atmospheric models. *Atmospheric Chemistry and Physics*, *11*(9), 4039–4072. https://doi.org/10.5194/acp-11-4039-2011

Albini, F. A. (1976). Estimating wildfire behavior and effects (Gen. Tech. Rep. INT-GTR-30). Ogden, UT: Intermountain Forest and range Experiment Station, USDA Forest Service.

Amante, C., & Eakins, B.W. (2009). ETOPO1 1 arc-minute global relief model: Procedures, data sources and analysis (NOAA Technical Memorandum NESDIS NGDC-24). Boulder, CO: National Geophysical Data Center, NOAA. https://doi.org/10.7289/V5C8276M

Andela, N., Morton, D. C., Giglio, L., Chen, Y., van der Werf, G. R., Kasibhatla, P. S., et al. (2017). A human-driven decline in global burned area. *Science*, *356*(6345), 1356–1362. https://doi.org/10.1126/science.aal4108

Andela, N., & van der Werf, G. R. (2014). Recent trends in African fires driven by cropland expansion and El Nino to La Nina transition. *Nature Climate Change*, *4*, 791–795. https://doi.org/10.1038/nclimate2313

Archibald, S., Staver, A. C., & Levin, S. A. (2012). Evolution of human-driven fire regimes in Africa. *Proceedings of the National Academy of Sciences of the United States of America*, *109*, 847–852. https://doi.org/10.1073/pnas.1118648109

Arora, V. K., & Boer, G. J. (2005). Fire as an interactive component of dynamic vegetation models. *Journal of Geophysical Research*, *110*, G02008. https://doi.org/10.1029/2005JG000042

Balch, J. K., Nepstad, D. C., & Curran, L. M. (2009). Pattern and process: Fire-initiated grass invasion at Amazon transitional forest edges. In M. Cochrane (Ed.), *Tropical fire ecology: Climate change, land use, and ecosystem dynamics* (pp. 481–502). Heidelberg, Germany: Springer-Verlag Berlin Heidelberg. https://doi.org/10.1007/978-3-540-77381-8

Barlow, J., Peres, C. A., Lagan, B. O., & Haugaasen, T. (2003). Large tree mortality and the decline of forest biomass following Amazonian wildfires. *Ecology Letters*, *6*(1), 6–8.

Beck, P. S. A., & Goetz, S. J. (2011). Satellite observations of high northern latitude vegetation productivity changes between 1982 and 2008: Ecological variability and regional differences. *Environmental Research Letters*, *6*. https://doi.org/10.1088/1748-3182/6/4/049501

Bond, W. J., Woodward, F. I., & Midgley, G. F. (2005). The global distribution of ecosystems in a world without fire. *New Phytologist*, *165*, 525–537.

Bond-Lamberty, B., Wang, C., & Gower, S. T. (2002). Aboveground and belowground biomass and sapwood area allometric equations for six boreal tree species of northern Manitoba. *Canadian Journal of Forest Research*, *32*(8), 1441–1450. https://doi.org/10.1139/x02-063

Bowman, D. M. J. S., Balch, J., Artaxo, P., Bond, W. J., Cochrane, M. A., D'Antonio, C. M., et al. (2011). The human dimension of fire regimes on Earth. *Journal of Biogeography*, *38*, 2223–2236. https://doi.org/10.1111/j.1365-2699.2011.02595.x

Bowman, D. M. J. S., Balch, J. K., Artaxo, P., Bond, W. J., Carlson, J. M., Cochrane, M. A., et al. (2009). Fire in the Earth system. *Science*, *324*, 481–484. https://doi.org/10.1126/science.1163886

Bowman, D. M. J. S., MacDermott, H. J., Nichols, S. C., & Murphy, B. P. (2014). A grass-fire cycle eliminates an obligate-seeding tree in a tropical savanna. *Ecology and Evolution*, *4*, 4185–4194. https://doi.org/10.1002/ece3.1285

Bradstock, R. A., Gill, A. M., & Williams, R. J. (Eds.) (2012). *Flammable Australia: Fire regimes, biodiversity and ecosystems in a changing world*. Clayton, Australia: CSIRO Publishing.

Brando, P. M., Balch, J. K., Nepstad, D. C., Morton, D. C., Putz, F. E., Coe, M. T., et al. (2014). Abrupt increases in Amazonian tree mortality due to drought-fire interactions. *Proceedings of the National Academy of Sciences of the United States of America*, *111*, 6347–6352. https://doi.org/10.1073/pnas.1305499111

Brando, P. M., Nepstad, D. C., Balch, J. K., Bolker, B., Christman, M. C., Coe, M., & Putz, F. E. (2012). Fire-induced tree mortality in a neotropical forest: The roles of bark traits, tree size, wood density and fire behavior. *Global Change Biology*, *18*, 630–641. https://doi.org/10.1111/j.1365-2486.2011.02533.x

Center for International Earth Science Information Network (CIESIN), Columbia University, & Centro Internacional de Agricultura Tropical (CIAT) (2005). *Gridded Population of the World version 3(GPWv3): Population density grids*. Palisades, NY: NASA Socioeconomic Data and Applications Center (SEDAC). https://doi.org/10.7927/H4XK8CG2

Chazdon, R. L. (2003). Tropical forest recovery: Legacies of human impact and natural disturbances. *Perspectives in Plant Ecology, Evolution and Systematics*, *6*(1–2), 51–71. https://doi.org/10.1078/1433-8319-00042

Chen, Y., Randerson, J. T., Morton, D. C., DeFries, R. S., Collatz, G. J., Kasibhatla, P. S., et al. (2011). Forecasting fire season severity in South America using sea surface temperature anomalies. *Science*, *334*, 787–791. https://doi.org/10.1126/science.1209472

Cochrane, M. A., Alencar, A., Schulze, M. D., Souza, C. M., Nepstad, D. C., Lefebvre, P., & Davidson, E. A. (1999). Positive feedbacks in the fire dynamic of closed canopy tropical forests. *Science*, *284*(5421), 1832–1835. https://doi.org/10.1126/science.284.5421.1832

Dormann, C. F., Elith, J., Bacher, S., Buchmann, C., Carl, G., Carré, G., et al. (2013). Collinearity: A review of methods to deal with it and a simulation study evaluating their performance. *Ecography*, *36*, 27–46. https://doi.org/10.1111/j.1600-0587.2012.07348.x

Epting, J., & Verbyla, D. (2005). Landscape-level interactions of prefire vegetation, burn severity, and postfire vegetation over a 16-year period in interior Alaska. *Canadian Journal of Forest Research*, *35*, 1367–1377. https://doi.org/10.1139/x05-060

Field, R. D., van der Werf, G. R., Fanin, T., Fetzer, E. J., Fuller, R., Jethva, H., et al. (2016). Indonesian fire activity and smoke pollution in 2015 show persistent nonlinear sensitivity to El Nino-induced drought. *Proceedings of the National Academy of Sciences of the United States of America*, *113*, 9204–9209. https://doi.org/10.1073/pnas.1524888113

Finegan, B. (1996). Pattern and process in neotropical secondary rain forests: The first 100 years of succession. *Trends in Ecology & Evolution*, *11*, 119–124. https://doi.org/10.1016/0169-5347(96)81090-1

Fisher, R. A., Muszala, S., Verteinstein, M., Lawrence, P., Xu, C., McDowell, N. G., et al. (2015). Taking off the training wheels: The properties of a dynamic vegetation model without climate envelopes, CLM4.5(ED). *Geoscientific Model Development*, *8*(11), 3593–3619. https://doi.org/10.5194/gmd-8-3593-2015

Flannigan, M. D., Krawchuk, M. A., de Groot, W. J., Wotton, B. M., & Gowman, L. M. (2009). Implications of changing climate for global wildland fire. *International Journal of Wildland Fire*, *18*, 483–507. https://doi.org/10.1071/WF08187

Forestry Canada Fire Danger Group (FCFDG). (1992). Development and structure of the Canadian forest fire behavior prediction system (Information Report ST-X-3). Ottawa, Canada: Science and Sustainable Development Directorate, Forestry Canada.

Gatti, L. V., Gloor, M., Miller, J. B., Doughty, C. E., Malhi, Y., Domingues, L. G., et al. (2014). Drought sensitivity of Amazonian carbon balance revealed by atmospheric measurements. *Nature*, *506*, 76–80. https://doi.org/10.1038/nature12957

Giglio, L., Csiszar, I., & Justice, C. O. (2006). Global distribution and seasonality of active fires as observed with the Terra and Aqua Moderate Resolution Imaging Spectroradiometer (MODIS) sensors. *Journal of Geophysical Research*, *111*, D14S08. https://doi.org/10.1029/2005JG000142

Giglio, L., Randerson, J. T., & van der Werf, G. R. (2013). Analysis of daily, monthly, and annual burned area using the fourth-generation Global Fire Emissions Database (GFED4). *Journal of Geophysical Research: Biogeosciences*, *118*, 317–328. https://doi.org/10.1002/jgrg.20042

Giglio, L., Randerson, J. T., van der Werf, G. R., Kasibhatla, P. S., Collatz, G. J., Morton, D. C., & DeFries, R. S. (2010). Assessing variability and long-term trends in burned area by merging multiple satellite fire products. *Biogeosciences*, *7*, 1171–1186. https://doi.org/10.5194/bg-7-1171-2010

Goetz, S. J., Fiske, G. J., & Bunn, A. G. (2006). Using satellite time-series data sets to analyze fire disturbance and forest recovery across Canada. *Remote Sensing of Environment*, *101*, 352–365. https://doi.org/10.1016/j.rse.2006.01.011

Goulden, M. L., McMillan, A. M. S., Winston, G. C., Rocha, A. V., Manies, K. L., Harden, J. W., & Bond-Lamberty, B. P. (2011). Patterns of NPP, GPP, respiration, and NEP during boreal forest succession. *Global Change Biology*, *17*, 855–871. https://doi.org/10.1111/j.1365-2486.2010.02274.x

Guariguata, M. R., & Ostertag, R. (2001). Neotropical secondary forest succession: Changes in structural and functional characteristics. *Forest Ecology and Management*, *148*(1–3), 185–206.

Hantson, S., Arneth, A., Harrison, S. P., Kelley, D. I., Prentice, I. C., Rabin, S. S., et al. (2016). The status and challenge of global fire modelling. *Biogeosciences*, *13*, 3359–3375. https://doi.org/10.5194/bg-13-3359-2016

Hantson, S., Padilla, M., Corti, D., & Chuvieco, E. (2013). Strengths and weaknesses of MODIS hotspots to characterize global fire occurrence. *Remote Sensing of Environment*, *133*, 152–159. https://doi.org/10.1016/j.rse.2012.12.004

Heilman, W. E., Liu, Y. Q., Urbanski, S., Kovalev, V., & Mickler, R. (2014). Wildland fire emissions, carbon, and climate: Plume transport, and chemistry processes. *Forest Ecology and Management*, *317*, 70–79. https://doi.org/10.1016/j.foreco.2013.02.001

Heward, H., Smith, A. M. S., Roy, D. P., Tinkham, W. T., Hoffman, C. M., Morgan, P., & Lannom, K. O. (2013). Is burn severity related to fire intensity? Observations from landscape scale remote sensing. *International Journal of Wildland Fire*, *22*, 910–918. https://doi.org/10.1071/WF12087

Hicke, J. A., Asner, G. P., Kasischke, E. S., French, N. H. F., Randerson, J. T., Collatz, G. J., et al. (2003). Postfire response of North American boreal forest net primary productivity analyzed with satellite observations. *Global Change Biology*, *9*(8), 1145–1157.

Hurrell, J. W., Hack, J. J., Shea, D., Caron, J. M., & Rosinski, J. (2008). A new sea surface temperature and sea ice boundary dataset for the Community Atmosphere Model. *Journal of Climate*, *21*, 5145–5153. https://doi.org/10.1175/2008JCLI2292.1

Hurrell, J. W., Holland, M. M., Gent, P. R., Ghan, S., Kay, J. E., Kushner, P. J., et al. (2013). The Community Earth System Model: A framework for collaborative research. *Bulletin of the American Meteorological Society*, *94*, 1339–1360. https://doi.org/10.1175/BAMS-D-12-00121.1

Hurtt, G. C., Frolking, S., Fearon, M. G., Moore, B., III, Shevliakova, E., Malyshev, S., et al. (2006). The Underpinnings of Land-use History: Three Centuries of Global Gridded Land-Use Transitions, Wood Harvest Activity, and Resulting Secondary Lands. *Global Change Biology*, *12*, 1208–1229. https://doi.org/10.1111/j.1365-2486.2006.01150.x

Ichoku, C., & Ellison, L. (2014). Global top-down smoke-aerosol emissions estimation using satellite fire radiative power measurements. *Atmospheric Chemistry and Physics*, *14*, 6643–6667. https://doi.org/10.5194/acp-14-6643-2014

Jacobson, M. Z. (2014). Effects of biomass burning on climate, accounting for heat and moisture fluxes, black and brown carbon, and cloud absorption effects. *Journal of Geophysical Research: Atmosphere*, *119*, 8980–9002.

Jin, Y. F., Randerson, J. T., Goetz, S. J., Beck, P. S. A., Loranty, M. M., & Goulden, M. L. (2012). The influence of burn severity on postfire vegetation recovery and albedo change during early succession in North American boreal forests. *Journal of Geophysical Research*, *117*, G01036. https://doi.org/10.1029/2011JG001886

Johnston, F. H., Henderson, S. B., Chen, Y., Randerson, J. T., Marlier, M., DeFries, R. S., et al. (2012). Estimated global mortality attributable to smoke from landscape fires. *Environmental Health Perspectives*, *120*, 695–701. https://doi.org/10.1289/ehp.1104422

Kaiser, J. W., Heil, A., Andreae, M. O., Benedetti, A., Chubarova, N., Jones, L., et al. (2012). Biomass burning emissions estimated with a global fire assimilation system based on observed fire radiative power. *Biogeosciences*, *9*, 527–554. https://doi.org/10.5194/bg-9-527-2012

Keeley, J. E. (2009). Fire intensity, fire severity and burn severity: A brief review and suggested usage. *International Journal of Wildland Fire*, *18*, 116–126. https://doi.org/10.1071/WF07049

Kelley, D. I., Harrison, S. P., & Prentice, I. C. (2014). Improved simulation of fire-vegetation interactions in the land surface processes and eXchanges dynamic global vegetation model (LPX-Mv1). *Geoscientific Model Development*, *7*, 2411–2433. https://doi.org/10.5194/gmd-7-2411-2014

Keyantash, J., & Dracup, J. A. (2002). The quantification of drought: An evaluation of drought indices. *Bulletin of the American Meteorological Society*, *83*(8), 1167–1180. https://doi.org/10.1175/1520-0477-83.8.1167

Kloster, S., Mahowald, N. M., Randerson, J. T., Thornton, P. E., Hoffman, F. M., Levis, S., et al. (2010). Fire dynamics during the 20th century simulated by the Community Land Model. *Biogeosciences*, *7*, 1877–1902. https://doi.org/10.5194/bg-7-1877-2010

Knorr, W., Dentener, F., Lamarque, J. F., Jiang, L., & Arneth, A. (2017). Wildfire air pollution hazard during the 21st century. *Atmospheric Chemistry and Physics*, *17*, 9223–9236. https://doi.org/10.5194/acp-17-9223-2017

Lamarque, J.-F., Bond, T. C., Eyring, V., Granier, C., Heil, A., Klimont, Z., et al. (2010). Historical (1850–2000) gridded anthropogenic and biomass burning emissions of reactive gases and aerosols: Methodology and application. *Atmospheric Chemistry and Physics*, *10*, 7017–7039. https://doi.org/10.5194/acp-10-7017-2010

Lenihan, J. M., & Bachelet, D. (2015). Historical climate and suppression effects on simulated fire and carbon dynamics in the conterminous United States. In D. Bachelet & D. Turner (Eds.), *Global vegetation dynamics: Concepts and applications in the MC1 modelGeophysical Monographs Series* (Vol. 214, pp. 17–30). Washington, DC: American Geophysical Union. https://doi.org/10.1002/9781119011705.ch2

Lenihan, J. M., Daly, C., Bachelet, D. & Neilson, R. P. (1998). Simulating broad-scale fire severity in a dynamic global vegetation model. *Northwest Science*, *72*, 91–101.

Li, F., Bond-Lamberty, B., & Levis, S. (2014). Quantifying the role of fire in the Earth system—part 2: Impact on the net carbon balance of global terrestrial ecosystems for the 20th century. *Biogeosciences*, *11*, 1345–1360. https://doi.org/10.5194/bg-11-1345-2014

Li, F., & Lawrence, D. M. (2017). Role of fire in the global land water budget during the twentieth century due to changing ecosystems. *Journal of Climate*, *30*, 1893–1908. https://doi.org/10.1175/JCLI-D-16-0460.1

Li, F., Levis, S., & Ward, D. S. (2013). Quantifying the role of fire in the Earth system—Part 1: Improved global fire modeling in the Community Earth System Model (CESM1). *Biogeosciences*, *10*, 2293–2314. https://doi.org/10.5194/bg-10-2293-2013

Li, F., Zeng, X. D., & Levis, S. (2012). A process-based fire parameterization of intermediate complexity in a Dynamic Global Vegetation Model. *Biogeosciences*, *9*, 2761–2780. https://doi.org/10.5194/bg-9-2761-2012

Liu, Y. Q., Goodrick, S., & Heilman, W. (2014). Wildland fire emissions, carbon, and climate: Wildfire-climate interactions. *Forest Ecology and Management*, *317*, 80–96. https://doi.org/10.1016/j.foreco.2013.02.020

Lu, Z., & Sokolik, I. N. (2013). The effect of smoke emission amount on changes in cloud properties and precipitation: A case study of Canadian boreal wildfires of 2007. *Journal of Geophysical Research: Atmosphere*, *118*, 11,777–11,793.

Luo, Y. Q., Randerson, J. T., Abramowitz, G., Bacour, C., Blyth, E., Carvalhais, N., et al. (2012). A framework for benchmarking land models. *Biogeosciences*, *9*, 3857–3874. https://doi.org/10.5194/bg-9-3857-2012

Ma, H. Y., Xie, S., Boyle, J. S., Klein, S. A., & Zhang, Y. (2013). Metrics and diagnostics for precipitation-related processes in climate model short-range hindcasts. *Journal of Climate*, *26*, 1516–1534.

Magi, B. I., Rabin, S., Shevliakova, E., & Pacala, S. (2012). Separating agricultural and non-agricultural fire seasonality at regional scales. *Biogeosciences*, *9*, 3003–3012. https://doi.org/10.5194/bg-9-3003-2012

Marlier, M. E., DeFries, R. S., Voulgarakis, A., Kinney, P. L., Randerson, J. T., Shindell, D. T., et al. (2013). El Nino and health risks from landscape fire emissions in Southeast Asia. *Nature Climate Change*, *3*, 131–136. https://doi.org/10.1038/nclimate1658

Marlon, J. R., Bartlein, P. J., Walsh, M. K., Harrison, S. P., Brown, K. J., Edwards, M. E., et al. (2009). Wildfire responses to abrupt climate change in North America. *Proceedings of the National Academy of Sciences of the United States of America*, *106*, 2519–2524. https://doi.org/10.1073/pnas.0808212106

Medeiros, M., & Miranda, H. (2008). Post-fire resprouting and mortality in cerrado woody plant species over a three-year period. *Edinburgh Journal of Botany*, *65*, 53–68.

Myhre, G., Shindell, D., Bréon, F.-M., Collins, W., Fuglestvedt, J., Huang, J., et al. (2013). Anthropogenic and natural radiative forcing. In *Climate change 2013: The physical science basis, IPCC the Fifth Assessment Report* (Chap. 8). Cambridge, UK: Cambridge University Press.

Neale, R. B., Chen, C.-C., Gettelman, A., Lauritzen, P. H., Park, S., Williamson, D. L., et al. (2012). Description of the NCAR Community Atmosphere Model (CAM 5.0) (NCAR Technical Note/TN-486+STR). Boulder, CO: National Center for Atmospheric Research.

Oleson, K. W., Lawrence, D. M., Bonan, G. B., Drewniak, B., Huang, M. Y., Koven, C. D., Levis, S., et al. (2013), Technical description of version 4.5 of the Community Land Model (CLM) (NCAR Technical Note/TN-503+STR). Boulder, CO: National Center for Atmospheric Research.

Pechony, O., & Shindell, D. T. (2009). Fire parameterization on a global scale. *Journal of Geophysical Research*, *114*(D16), D16115. https://doi.org/10.1029/2009JD011927.

Pechony, O., & Shindell, D. T. (2010). Driving forces of global wildfires over the past millennium and the forthcoming century. *Proceedings of the National Academy of Sciences of the United States of America*, *107*, 19,167–19,170. https://doi.org/10.1073/pnas.1003669107

Pfeiffer, M., Spessa, A., & Kaplan, J. O. (2013). A model for global biomass burning in preindustrial time: LPJ-LMfire (v1.0). *Geoscientific Model Development*, *6*, 643–685. https://doi.org/10.5194/gmd-6-643-2013

Piani, C., Weedon, G. P., Best, M., Gomes, S. M., Viterbo, P., Hagemann, S., & Haerter, J. O. (2010). Statistical bias correction of global simulated daily precipitation and temperature for the application of hydrological models. *Journal of Hydrology*, *395*, 199–215. https://doi.org/10.1016/j.jhydrol.2010.10.024

Prentice, S. A., & Mackerras, D. (1977). The ratio of cloud to cloud-ground lightning flashes in thunderstorms. *Journal of Applied Meteorology*, *16*(5), 545–550. https://doi.org/10.1175/1520-0450(1977)016<0545:troctc>2.0.co;2

Qian, T. T., Dai, A., Trenberth, K. E., & Oleson, K. W. (2006). Simulation of global land surface conditions from 1948 to 2004. Part I: Forcing data and evaluations. *Journal of Hydrometeorology*, *7*, 953–975.

Randerson, J. T., Chen, Y., van der Werf, G. R., Rogers, B. M., & Morton, D. C. (2012). Global burned area and biomass burning emissions from small fires. *Journal of Geophysical Research*, *117*, G04012. https://doi.org/10.1029/2012jg002128

Randerson, J. T., Liu, H., Flanner, M. G., Chambers, S. D., Jin, Y., Hess, P. G., et al. (2006). The impact of boreal forest fire on climate warming. *Science*, *314*(5802), 1130–1132. https://doi.org/10.1126/science.1132075

Richards, M. B., & Lamont, B. B. (1996). Post-fire mortality and water relations of three congeneric shrub species under extreme water stress—A tradeoff with fecundity? *Oecologia*, *107*(1), 53–60. https://doi.org/10.1007/BF00582234

Rogers, B. M., Soja, A. J., Goulden, M. L., & Randerson, J. T. (2015). Influence of tree species on continental differences in boreal fires and climate feedbacks. *Nature Geoscience*, *8*, 228–234. https://doi.org/10.1038/ngeo2352

Running, S. W. (2008). Climate change - ecosystem disturbance, carbon, and climate. *Science*, *321*(5889), 652–653. https://doi.org/10.1126/science.1159607

Rydgren, K., Okland, R. H., & Hestmark, G. (2004). Disturbance severity and community resilience in a boreal forest. *Ecology*, *85*(7), 1906–1915. https://doi.org/10.1890/03-0276

Teutschbein, C., & Seibert, J. (2012). Bias correction of regional climate model simulations for hydrological climate-change impact studies: Review and evaluation of different methods. *Journal of Hydrology*, *456*, 12–29.

Thonicke, K., Spessa, A., Prentice, I. C., Harrison, S. P., Dong, L., & Carmona-Moreno, C. (2010). The influence of vegetation, fire spread and fire behavior on biomass burning and trace gas emissions: Results from a process-based model. *Biogeosciences*, *7*, 1991–2011. https://doi.org/10.5194/bg-7-1991-2010

van der Werf, G. R., Randerson, J. T., Giglio, L., Collatz, G. J., Mu, M., Kasibhatla, P. S., et al. (2010). Global fire emissions and the contribution of deforestation, savanna, forest, agricultural, and peat fires (1997–2009). *Atmospheric Chemistry and Physics*, *10*, 11,707–11,735. https://doi.org/10.5194/acp-10-11707-2010

van der Werf, G. R., Randerson, J. T., Giglio, L., van Leeuwen, T. T., Chen, Y., Rogers, B. M., et al. (2017). Global fire emissions estimates during 1997–2016. *Earth System Science Data*, *9*, 697–720. https://doi.org/10.5194/essd-9-697-2017

van Leeuwen, T. T., van der Werf, G. R., Hoffmann, A. A., Detmers, R. G., Rücker, G., French, N. H. F., et al. (2014). Biomass burning fuel consumption rates: A field measurement database. *Biogeosciences*, *11*, 7305–7329. https://doi.org/10.5194/bg-11-7305-2014

van Wagner, C. E. (1969). A simple fire-growth model. *The Forestry Chronicle*, *45*, 103–104. https://doi.org/10.5558/tfc45103-2

Venevsky, S., Thonicke, K., Sitch, S., & Cramer, W. (2002). Simulating fire regimes in human-dominated ecosystems: Iberian Peninsula case study. *Global Change Biology*, *8*(10), 984–998. https://doi.org/10.1046/j.1365-2486.2002.00528.x

Veraverbeke, S., Rogers, B. M., Goulden, M. L., Jandt, R. R., Miller, C. E., Wiggins, E. B., & Randerson, J. T. (2017). Lightning as a major driver of recent large fire years in North American boreal forests. *Nature Climate Change*, *7*, 529–534. https://doi.org/10.1038/nclimate3329

Vila, M., Lloret, F., Ogheri, E., & Terradas, J. (2001). Positive fire-grass feedback in Mediterranean Basin woodlands. *Forest Ecology and Management*, *147*(1), 3–14. https://doi.org/10.1016/S0378-1127(00)00435-7

Viovy, N. (2013), CRUNCEP Version 4—Atmospheric forcing data for the Community Land Model. http://dods.extra.cea.fr/data/p529viov/cruncep/. Accessed 8 Jul 2017.

Wang, C., Zhang, L., Lee, S. K., Wu, L., & Mechoso, C. R. (2014). A global perspective on CMIP5 climate model biases. *Nature Climate Change*, *4*, 201–205. https://doi.org/10.1038/nclimate2118

Ward, D. S., Kloster, S., Mahowald, N. M., Rogers, B. M., Randerson, J. T., & Hess, P. G. (2012). The changing radiative forcing of fires: Global model estimates for past, present and future. *Atmospheric Chemistry and Physics*, *12*, 10,857–10,886. https://doi.org/10.5194/acp-12-10857-2012

Westerling, A. L., Hidalgo, H. G., Cayan, D. R., & Swetnam, T. W. (2006). Warming and earlier spring increase western US forest wildfire activity. *Science*, *313*(5789), 940–943. https://doi.org/10.1126/science.1128834

Wooster, M. J., & Zhang, Y. H. (2004). Boreal forest fires burn less intensely in Russia than in North America. *Geophysical Research Letters*, *31*, L20505. https://doi.org/10.1029/2004GL020805

Yang, J., Tian, H. Q., Tao, B., Ren, W., Kush, J., Liu, Y. Q., & Wang, Y. H. (2014). Spatial and temporal patterns of global burned area in response to anthropogenic and environmental factors: Reconstructing global fire history for the 20th and early 21st centuries. *Journal of Geophysical Research: Biogeosciences*, *119*, 249–263. https://doi.org/10.1002/2013jg002532

Yang, J., Tian, H. Q., Tao, B., Ren, W., Pan, S. F., Liu, Y. Q., & Wang, Y. H. (2015). A growing importance of large fires in conterminous United States during 1984-2012. *Journal of Geophysical Research: Biogeosciences*, *120*, 2625–2640. https://doi.org/10.1002/2015jg002965

Yue, X., Mickley, L. J., Logan, J. A., & Kaplan, J. O. (2013). Ensemble projections of wildfire activity and carbonaceous aerosol concentrations over the western United States in the mid-21st century. *Atmospheric Environment*, *77*, 767–780. https://doi.org/10.1016/j.atmosenv.2013.06.003

Zeng, T., Wang, Y. H., Yoshida, Y., Tian, D., Russell, A. G., & Barnard, W. R. (2008). Impacts of prescribed fires on air quality over the southeastern United States in spring based on modeling and ground/satellite measurements. *Environmental Science and Technology*, *42*, 8401–8406. https://doi.org/10.1021/es800363d

Zhang, X. Y., Drake, N. A., Wainwright, J., & Mulligan, M. (1999). Comparison of slope estimates from low resolution DEMs: Scaling issues and a fractal method for their solution. *Earth Surface Processes and Landforms*, *24*(9), 763–779. https://doi.org/10.1002/(SICI)1096-9837(199908)24:9<763::AID-ESP9>3.0.CO;2-J

Zimmermann, J., Higgins, S. I., Grimm, V., Hoffmann, J., & Linstadter, A. (2010). Grass mortality in semi-arid savanna: The role of fire, competition and self-shading. *Perspectives in Plant Ecology*, *12*, 1–8. https://doi.org/10.1016/j.ppees.2009.09.003